Max Planck Institute for
Gravitational Physics
(Albert Einstein Institute)

LISA Pathfinder Mission Extension Report for the German Contribution

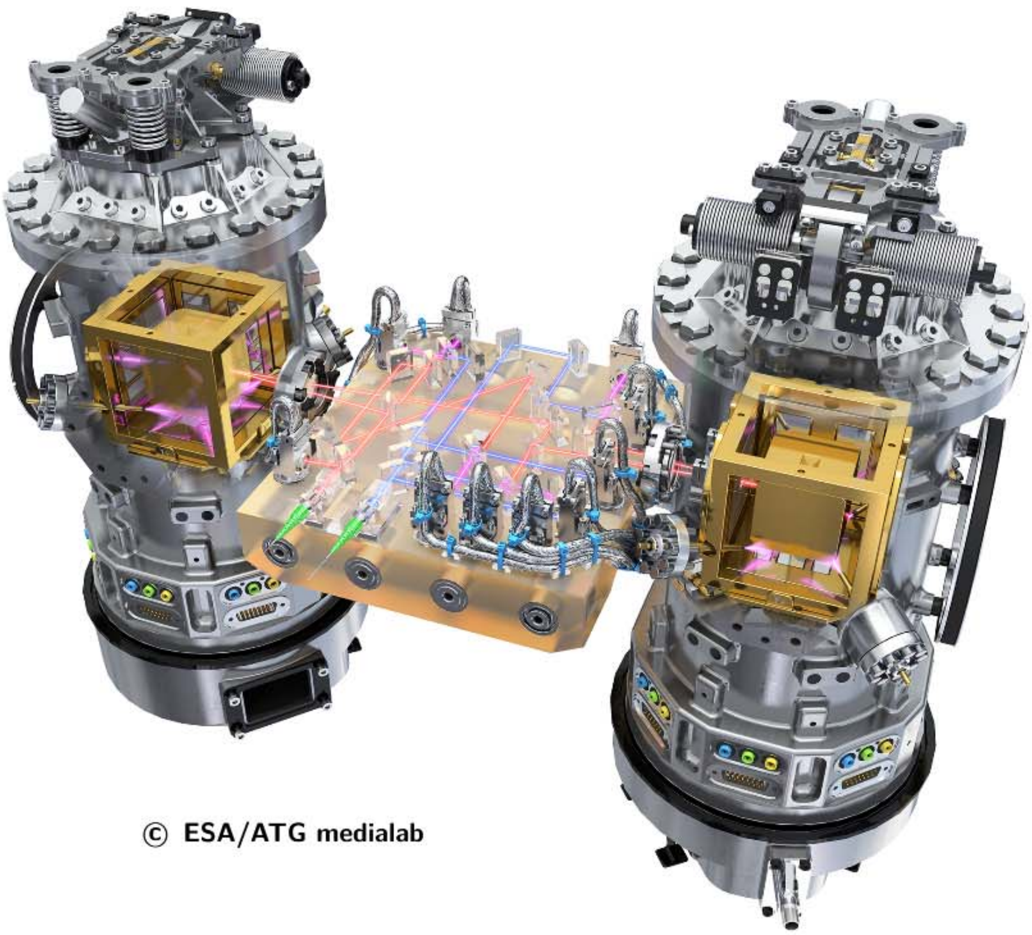

© ESA/ATG medialab

LPF Team, Germany

Title: LISA Pathfinder Mission Extension Report for the German Contribution
Release date: February 3, 2020
Issue: 1

Organisations:
Max Planck Institute for Gravitational Physics
Albert Einstein Institute
Airbus DS GmbH
OHB System AG
Tesat Spacecom GmbH & Co. KG

For the Laser Interferometer Space Antenna (LISA)

List of Authors

Name	Organisation
Heather Audley	AEI
Michael Born	AEI
Karsten Danzmann	AEI
Marie-Sophie Hartig	AEI
Gerhard Heinzel	AEI
Martin Hewitson	AEI
Nikolaos Karnesis	AEI
Brigitte Kaune	AEI
Sarah Paczkowski	AEI
Jens Reiche	AEI
Gudrun Wanner	AEI
Lennart Wissel	AEI
Andreas Wittchen	AEI

Contents

List of Acronyms

ADC	Analogue to Digital Convertor
AEI	Albert Einstein Institute
ao	Analysis Object
AOM	Acousto-Optic Modulator
APC	AstroParticule et Cosmologie, Université Paris Diderot
ASD	Amplitude Spectral Density
ASU	Astrium UK
BH92	Blackmann-Harris-92
CAD	Computer Aided Design
CLG	Closed-Loop Gain
CLTF	Closed-Loop Transfer Function
CMM	Coordinate Measurement Machine
CQP	Calibrated Quadrant Photodiode
DAC	Digital to Analogue Convertor
DC	Direct Current
DDS	Data Disposition System
DFACS	Drag-Free and Attitude Control System
DFT	Discrete Fourier transform
DMU	Data Management Unit
DOY	Day of year
DPS	Differential Power Sensing
DRS	Disturbance Reduction System
DWS	Differential Wavefront Sensing
eLISA	Evolved LISA
ELITE	European LIsa TEchnology
EM	Engineering Model
EMP	Experimental Master Plan
ESA	European Space Agency
FF	Fast Frequency
FFT	Fast Fourier transform
FIOS	Fibre Injector Optical Sub-Assembly
FIR	Finite Impulse Response
FM	Flight Model

FP	Fast Power
FPGA	Field Programmable Gate Array
FT	Fourier Transform
GRS	Gravitational Reference Sensor
GUI	Graphical User Interface
HR	High Resolution
IABG	Industrieanlagen-Betriebsgesellschaft mbH
ICE	Instrument Configuration Evaluation
IDL	Interferometer Data Log
IFO	Interferometer
IGR	Institute for Gravitational Research, University of Glasgow
IIR	Infinite Impulse Response
ITO	Indium Tin Oxide
KT	Kaiser Threde
L_1	Lagrange point 1
LA	Laser Assembly
LA PFM	Laser Assembly Pre-Flight Model
LCA	LTP Core Assembly
LCU	Laser Control Unit
LISA	Laser Interferometer Space Antenna
LMU	Laser Modulation Unit
LPF	LISA Pathfinder
LPSD	Logarithmic frequency axis Power Spectral Density
LTP	LISA Technology Package
LTPDA	LISA Technology Package Data Analysis
MAD	Median Absolute Deviation
MBW	measurement bandwidth
MCMC	Markov Chain Monte-Carlo
MOC	Mission Operations Centre
NASA	National Aeronautics and Space Administration
NPRO	Non-Planar Ring Oscillator
NTE	NTE Sener with IEEC, Barcelona
OB	Optical Bench
OBC	Onboard Computer

OBF	Optical Bench Frame
OBI	Optical Bench Interferometer
OGSE	On-ground Support Equipment
OLG	Open-Loop Gain
OLTF	Open-Loop Transfer Function
OMS	Optical Metrology System
OPD	Optical Pathlength Difference
OSTT	On-Station Thermal Tests
PD	Photodiode
PFM	Pre-Flight Model
PLL	Phase Locked Loop
PM	Phasemeter
PPS	Pulse per second
PSD	Power Spectral Density
PT	Phase Tracking
PZT	Piezo-electric Transducer
QPD	Quadrant Photodiode
RAM	Random Access Memory
RF	Radio Frequency
RIN	Relative Intensity Noise
RLU	Reference Laser Unit
RMS	Root Mean Square
RPN	Relative Power Noise
SBDFT	Single-Bin Discrete Fourier Transform
SC	Spacecraft
S/C	Spacecraft
SDM	Science Data Mode
SDP	System Data Pool
SEPD	Single Element Photodiode
SF	Slow Frequency
SF	Slow Frequency
SID	System Identification
SMART-2	Small Missions for Advanced Research in Technology
SNR	Signal to Noise Ratio

SP	Slow power
SSC	Source Sequence Counter
SSM	State Space Model
SSMM	Solid-state Mass Memory
ST-7	Space Technology-7
STOC	Science Technology Operations Centre
TC	Telecommand
TIA	Trans-Impedance Amplifier
TM	Test Mass
TN	Technical Note
TTL	Tilt-To-Length
UOB	University of Birmingham
URLA	very low actuation authority
w.r.t	with respect to

1 Extension of the LISA Pathfinder mission

1.1 Background information and scope of this report

Due to the excellent performance and results of LISA Pathfinder (LPF) in the nominal mission duration, it was decided to extend the mission by half a year: from December 2016 to June 2017. This allowed to further observe how the Brownian force noise decreased over time and study other contributing noise sources by performing a multitude of additional experiments. This document presents the work of the German LPF team during this mission extension. The report itself is a direct continuation of the 'LPF final report for the German contribution to the nominal mission' [1] and knowledge of this document is assumed here. In particular, introductions to the LISA Pathfinder mission and interferometry are not repeated here and are to be found in [1].

1.2 Overview of the mission extension

Already at the beginning of the nominal LPF mission starting from March 2016 an important milestone was reached [2]: The residual test mass acceleration could be measured to be better than $(5.2 \pm 0.1)\,\mathrm{fm/s^2/\sqrt{Hz}}$ and interferometer displacement readout noise of $(34.8 \pm 0.3)\,\mathrm{fm/\sqrt{Hz}}$ which was significantly better than the mission requirements. In the frequency range from 0.7 to 20 mHz, the acceleration noise was dominated by Brownian noise of the residual gas particles surrounding the test masses. Due to continuous venting to space, this noise decreased gradually. The extended LPF mission then allowed to measure below the LISA requirement (see red curve in Fig 1.1).

This impressive low noise performance was, however, not just resulting from the long investigations, which were possible due to the mission extension, and a decrease in Brownian force noise due to continuous venting to space. In addition, the applied electrostatic actuation force could be calculated more precisely, resulting in a more precise estimate of the differential TM acceleration. Moreover, the measured residual acceleration time series could be corrected for an inertial force from the SC rotation [3]. Apart from measuring the residual acceleration, a multitude of investigations was performed during the mission extension to deepen the understanding of all LPF subsystems. For example, a noisy force on the TMs results from a mixing of noisy charge with stray potentials and, vice versa, a static TM charge couples to noisy stray voltages. These effects have been characterised by estimating the TM charge by applying known voltage modulations and by estimating the uncompensated potentials as part of the mission extension. Consequently, these effects have been minimised by setting compensation voltages and discharging the TMs. The LPF performance is by far not limited by residual acceleration obtained via these mechanisms [6]. Furthermore, the mission extension enabled us to assess the GRS electrostatic sensing noise performance over a longer time and to refine the corresponding sensing noise model [7]. The extended mission duration

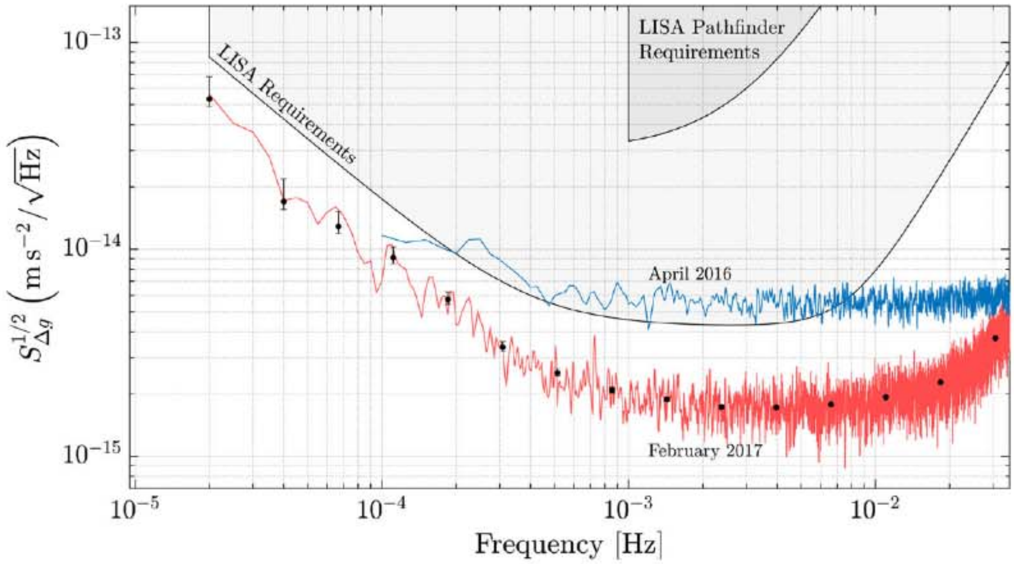

Figure 1.1: Reprint of FIG. 1 of [3]. ASD of parasitic differential acceleration of LPF test masses as a function of the frequency. Data refer to an ∼ 13 day long run taken at a temperature of 11°C. The red, noisy line is the ASD estimated with the standard periodogram technique averaging over 10, 50% overlapping periodograms each 2×10^5 s long. The data points with error bars are uncorrelated, averaged estimates calculated as explained in the text. For comparison, the blue noisy line is the ASD published in Ref. [2]. Data are compared with LPF requirements [4] and with LISA requirements taken from Ref. [5]. Fulfilling requirements implies that the noise must be below the corresponding shaded area at all frequencies. LISA requirements below 0.1 mHz must be considered just as goals [5].

gave the possibility to repeat instrument characterisation to identify degradations that could influence the LISA performance in its 5+ years lifetime. Results of such investigations of the OMS are presented in this report (see especially Section 1.3 and Chapter 2). Other examples are the charge management system. It counteracts charging due to particles from galactic cosmic rays and solar energetic particles by photoemission. This is different to other space missions which used, simply speaking, a discharging wire. Such a mechanical connection would not be possible with the low residual acceleration level on LPF. During the mission extension, estimates of the generated electrons per photon, the so-called apparent yield, have been continued [8].

The extended duration also gave insights into the space environment that has to be taken into account for the LISA design even though the orbits will be different to LPF orbit around L1 [9, 10, 11].

After the successful nominal mission period the extension also allowed to perform more risky experiments. The TM grab and release mechanism was used several times to optimise the procedure and verify the repeatability. Furthermore, the whole spacecraft was cooled down to 11°C which reduced the pressure in the enclosures of the test masses.

At the end of the extended mission period the final command was sent on the 18th of July

2017. The deactivated LPF S/C is now on a long-term stable parking orbit around the sun.

1.3 Overview of the OMS performance during the mission extension

The OMS worked reliably throughout the mission and also the mission extension. By being able to run a set of dedicated and extensive experiments that were continued in the extension, we deepened our understanding of the noise behaviour. This allowed us to build a model that is now being applied for the design and development of the LISA optical metrology.

We were able to show that the total sensing noise consisted of the following contributing noise sources;

- Phasemeter readout noise (electronics and ADC);
- Laser frequency noise;
- Laser Relative Intensity Noise (RIN);
- Shot noise.

This analysis is described in detail in [12].

Additional major influences to the OMS that are not considered sensor noises themselves but have been observed are originating from crosstalk: i.e. angular and lateral motion cross-coupling to the longitudinal readout.

Experiments targeting the noise sources mentioned above and other detailed system behaviour analysis are explained in the following sections. This was made possible due to the excellent performance, allowing us to investigate noise sources that were well below the requirements.

We found that the overall mission behaviour stayed below the o_{12} requirement (representing the main differential test mass to test mass measurement) of

$$S_{o_{12}}^{\frac{1}{2}} \leq 9\,\mathrm{pm}/\sqrt{\mathrm{Hz}} \times \sqrt{1 + (3\,\mathrm{mHz}/f)^4} \tag{1.1}$$

for nominal operational modes of the spacecraft. Figure 1.2 shows the measured behaviour during the mission extension. Here we also include data from the so called cooldown, i.e. low operating temperatures of the spacecraft (see data in grey areas). The behaviour is still below the requirements, but shows more excess noise and apparent non-stationary behaviour and is therefore still under investigation.

Limitations of the noise modelling When the noise model mentioned above and described in [12] was derived and verified, a number of limitations for the verification process were observed:

- The data was downloaded after a number of downsampling procedures took place aboard the spacecraft. This has likely introduced a certain but unknown level of aliasing in the high frequency band, which we need to use to assess the noise spectrum and model the physical noise sources. At lower frequencies we measured real test mass motion and therefore could not observe the sensor limit directly.

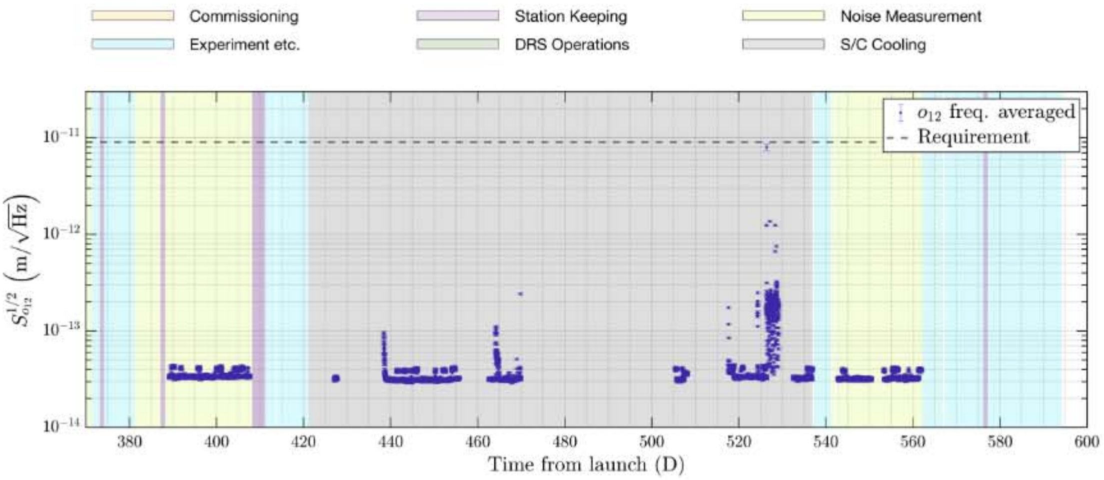

Figure 1.2: This plot shows the average OMS noise behaviour in the mission extension for the differential test mass to test mass measurement during selected times. The measured noise is below the requirements. Each point corresponds to 12 min of data, with an averaged spectral density in an approximately flat band between 1.2 Hz to 2.8 Hz. The transients are still under investigation. Note that we also included data that was measured during non-nominal operating conditions. Certain segments contain no data, since there were additional experiments taking place or non-nominal modes of spacecraft operations.

- The data from each QPD segment was already combined aboard LPF and no single quadrant information was available.
- No direct RIN measurement was possible in-flight.
- Only limited information about the ADC noise was available.
- It was difficult to estimate how polarization noise affected the system.

Nevertheless, our noise model explains all nominal science conditions that appeared in-flight reasonably well. Towards lower frequencies, the measured relative distance o_{12} is dominated by true motion and thus the sensing noise is not directly accessible. For more information see [12].

1.4 Science operations during the mission extension

For the mission extension we were able to continue the workflow that had been developed during the main mission and that took advantage of a close collaboration with all involved parties, especially the STOC at Darmstadt. This has been described in the first report about the main mission, see [1].

For the mission extension, we were able to design new experiments, based on data from the main mission, that continued to be being tested with the LPF simulator from ESA, thus allowing us to identify possible problems and mitigate them in close collaboration with

ESA engineers and scientists from the LPF community, before they were uploaded and run aboard the spacecraft.

Keeping the procedures quite similar to the main mission allowed us to build on the knowledge of the previous mission results and to deepen our understanding of the LPF experiment. Therefore the following sections describe experiments and tasks that were performed by members of the AEI LPF team, alongside the LPF collaboration, during the mission extension.

2 Longterm monitoring of PD sensitivity and TM reflectivity

2.1 Introduction

The interferometric readout - providing the main science measurement on LPF - is obtained by processing the power measured on the several PDs. Therefore, the longterm stability of the PDs is of major interest. LPF offered the opportunity to monitor the PD-power-measurements in a LISA-like environment.

As described in more detail in the final report of the nominal mission [1], especially the PD-responsivity and the TM-reflectivity are of interest.

The PDs as electro-optical components are particularly sensitive to cosmic rays and the TM-reflectivity directly impacts the force noise.

The mission extension phase was of great advantage to the monitoring experiments because the extended monitoring-duration allows for more reliable extrapolation to a LISA-like lifetime.

Monitoring these parameters has one great advantage - they are indistinguishable by the PD-measurements alone: The measured power is linearly dependent on photodiode-responsivity, TM-reflectivity and laser-power. Therefore, it is impossible to distinguish between these quantities by the measurement itself, even if there are many of them. To break the linear dependency, two experiments were designed to isolate the observables, as described briefly in the following.
A more detailed description of the experimental design can be found in the final mission report [1].

2.2 Experimental planning

TM-reflectivity

The TM-reflectivity R_{TM} can be retrieved from a combination of single-beam power measurements $\Sigma_i(P_M=0)$ and $\Sigma_i(P_R=0)$:

$$\Sigma_i(P_M=0) = P_R \cdot L_{iR} \cdot \eta_i \tag{2.1}$$

$$\Sigma_i(P_R=0) = P_M \cdot L_{iM} \cdot R_{TMj} \cdot \eta_i \tag{2.2}$$

$$R_{TM1} = \frac{\Sigma_1(P_R=0) \cdot \Sigma_R(P_M=0)}{\Sigma_1(P_M=0) \cdot \Sigma_R(P_R=0)} \cdot \frac{L_{1R} \cdot L_{RM}}{L_{1M} \cdot L_{RR}} \tag{2.3}$$

$$R_{TM2} = \frac{\Sigma_{12}(P_R=0) \cdot \Sigma_1(P_M=0)}{\Sigma_{12}(P_M=0) \cdot \Sigma_1(P_R=0)} \cdot \frac{L_{12R} \cdot L_{1M}}{L_{12M} \cdot L_{1R}} \,. \tag{2.4}$$

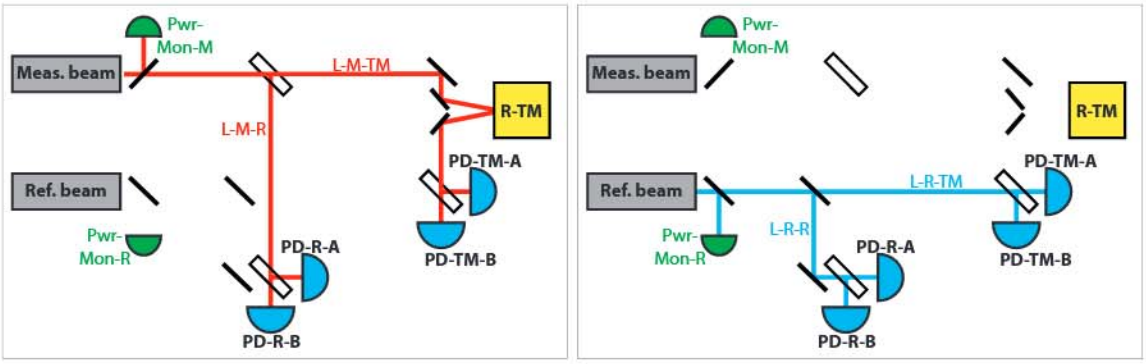

Figure 2.1: Beam-paths of reference and measurement beam on a simplified OB. Optical properties of mirrors and beam-splitters are combined in the factors L_{iM}/L_{iR}

In equation (2.3) and (2.4) the PD-responsivities η_i as well as the beam power P_R and P_M cancel, which isolates the TM-reflectivity.

The losses at mirrors and beam-splitters in a particular beam-path L_{iM} and L_{iR} are assumed to be constant over the mission duration.

PD-responsivity

To further break the linear dependency of PD-responsivity and laser-power, the power-independent interferometric readout is used: LPF is a high precision accelerometer - therefore, the radiation pressure to the TMs can be measured with enough accuracy to retrieve the applied power.

The applied force to the TMs is given by equation (2.5),

$$F_{\mathrm{TM1}} + F_{\mathrm{TM2}} = (1 + R_{\mathrm{TM1}}) \cdot \frac{P_{\mathrm{TM1}}}{\mathrm{c}} + (1 + R_{\mathrm{TM2}}) \cdot \frac{P_{\mathrm{TM2}}}{\mathrm{c}} \tag{2.5}$$

with the speed of light c.

Next to the radiation pressure there are more sources of static force to the TMs, which are counter-acted with a constant voltage to the TM. Therefore the power of the beam P_M, hitting the TMs, was modulated to isolate the contribution in frequency. The power-modulation combined with the constant voltage results in a back-and-forth displacement of the TMs.

LPFs analogue power control-loop only allowed for a square-wave modulation. A simplified scheme of the experiment together with a time-series of the actual measurement can be seen in figure (2.2). Conveniently this also provided signal at different frequencies - the several odd harmonics of the modulation frequency.

The modulated power is given by equation (2.6) and the resulting differential acceleration by equation (2.7),

$$\Sigma_i(@\, f_{\mathrm{mod}}) = P_{\mathrm{TMi}} \cdot L_{TMi-PDi} \cdot \eta_i \tag{2.6}$$

$$\Delta_g(@\, f_{\mathrm{mod}}) = (1 + R_{TM1}) \cdot \frac{P_{TM1}}{c \cdot m_{TM1}} + (1 + R_{TM2}) \cdot \frac{P_{TM2}}{c \cdot m_{TM2}} \; . \tag{2.7}$$

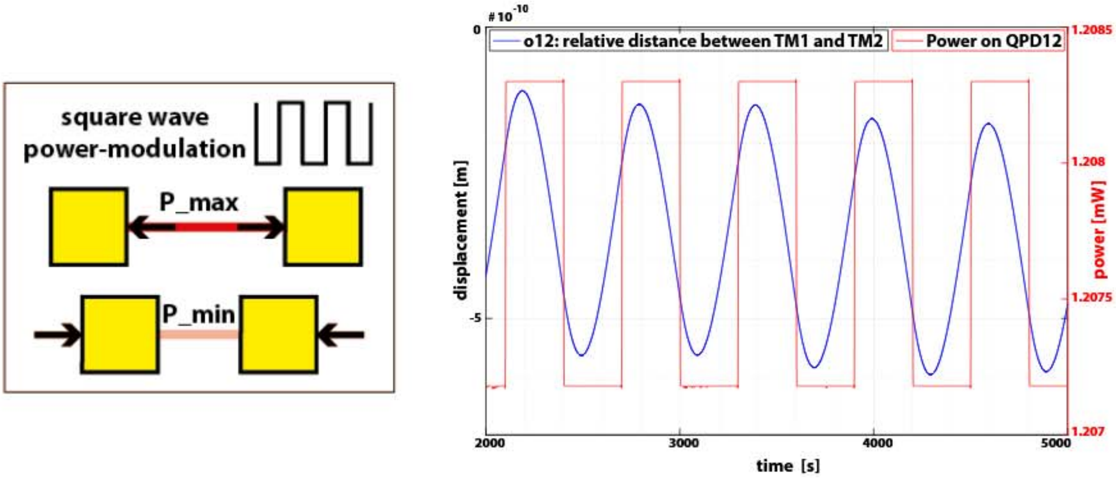

Figure 2.2: Radiation pressure modulation experiment. **Left:** scheme of the power - modulation and the implied TM-displacement. **Right:** measurement of modulated power and resulting TM-displacement.

with the TM-mass m_{TM}

The PD-responsivity η_i can be deduced by:

$$\begin{aligned}\eta_i =&(1+R_{TM1}) \cdot \frac{\Sigma_i(@\, f_{\text{mod}})}{\Delta_g(@\, f_{\text{mod}}) \cdot L_{TM1-PDi} \cdot c \cdot m_{TM1}} \\ &+ (1+R_{TM2}) \cdot \frac{\Sigma_i(@\, f_{\text{mod}})}{\Delta_g(@\, f_{\text{mod}}) \cdot L_{TM2-PDi} \cdot c \cdot m_{TM2}} \,. \end{aligned} \tag{2.8}$$

2.3 TM-reflectivity

For the computation of TM-reflectivity the single beam powers need to be measured. Hence, the beams were turned off one after another. Of course this could only be done during modes with GRS-control, because there is no interferometric readout.

Therefore most of these investigations were run during station keeping, so that no other experiments were disturbed.

Luckily the single beam powers were also needed for the analysis of spot positions on the PDs. The shared use of the data increases the outcome of the experiment and justifies the number of short measurements.

The so-called cool-down-phase was of special interest, because the temperature of the whole satellite was cooled down by several degrees. During this phase the beam-power-investigation was performed more frequently, to monitor the impact of temperature on spot positions.

All of the investigations could be used for determination of the TM-reflectivity. The gaps between two individual investigations last from an hour up to several days, as can be seen by the instants in time of all beam-power investigations, shown in figure (2.3).

In total there were 87 individual investigations from which 25 were taken during mission extension.

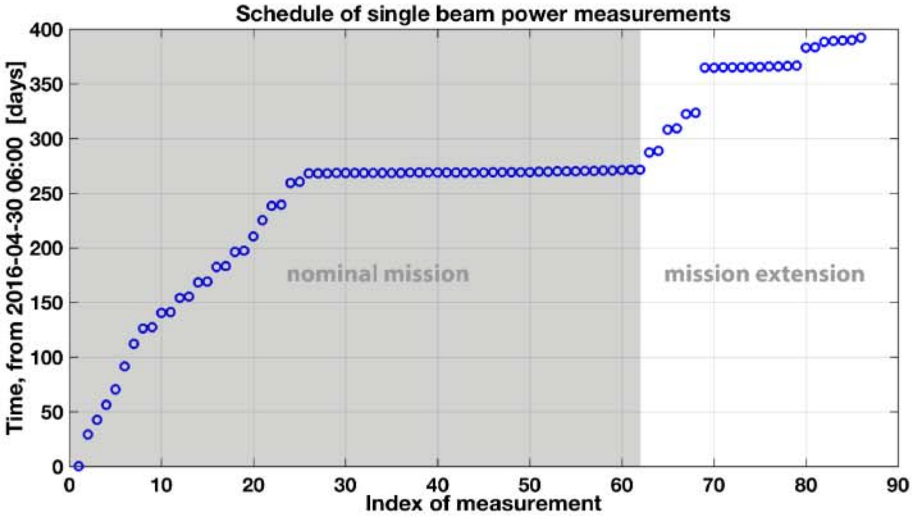

Figure 2.3: Schedule of all single beam power investigations, performed during flight of LPF. The last 26 investigations correspond to mission extension. The investigations with index 26 to 62 were taken more frequently during the so called "cool-down" phase.

For the analysis of spot positions 10 Hz-data was needed. Furthermore the power on the single quadrants of each QPD was needed, which gives 8 diodes times 4 quadrants, so 32 power-measurements times two beams. Due to this large amount of data, the power of the different diodes could not be recorded at the same time. Therefore the power of all quadrants in one interferometer was recorded for 1 minute. This was repeated for all other diodes and then for the other beam. A time-series of a typical investigation can be seen in figure (2.4). This plot was already shown in the nominal mission report [1] and is shown in here only to increase the readability.

In equation (2.3) and (2.4) ideally all laser-power-noise cancels. Unfortunately, as described above, the individual power-measurements on the different diodes could not be recorded at the same time. Therefore the TM-reflectivity could not be computed for each individual sample but only with the average power per investigation, giving one TM-reflectivity measurement point. By this of course the power-noise does not easily cancel any more. The impact of very high power noise is limited due to averaging of 10 Hz-data for one minute and the very low frequency noise is irrelevant due to the comparably short duration of one measurement (measurement duration of less than five minutes per beam).

Hence, only power-noise at frequencies in between these upper and lower limits is relevant to this measurement. But, luckily the power on LPF was stable enough, so that the measurement accuracy is not limited by this.

Figure (2.5) shows the average power of each investigation in the whole mission, exemplary for two selected channels per beam.

As already seen in the nominal mission, the measured power is affected by high power-noise. Figure (2.5) shows the channel with highest and lowest detected power-noise per beam.

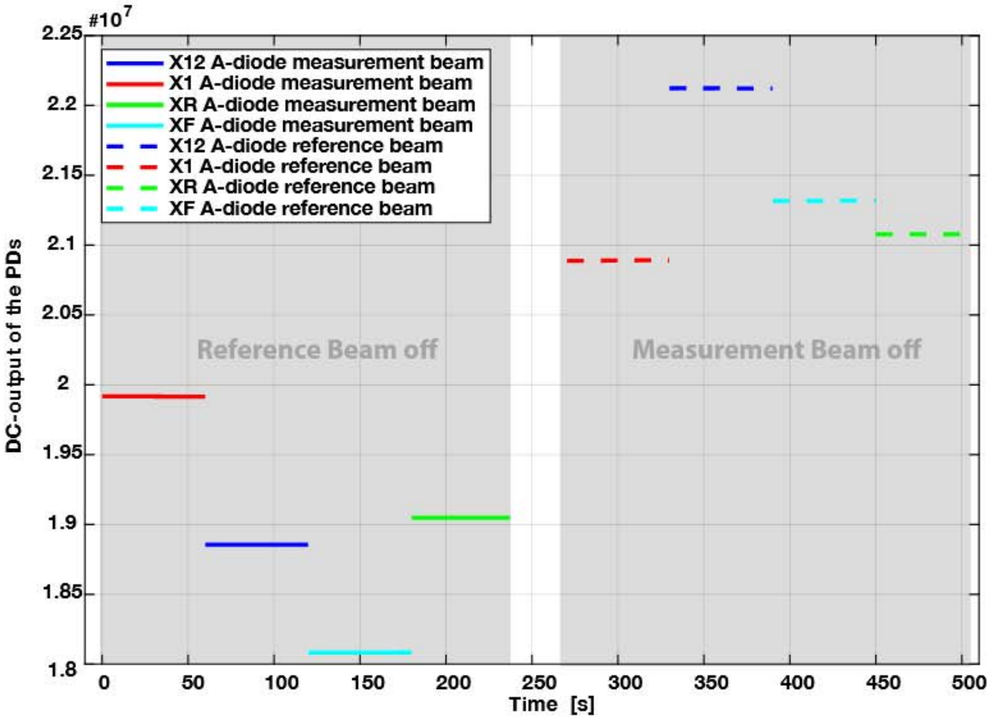

Figure 2.4: Time-series of a single-beam power investigation. The beam-power was measured individually for the four interferometers. One minute of data was gathered for each diode.

The source of this unexpected noise could be identified as polarisation-instabilities that became part of a new investigation - described in the following.

Since the noise was neither common mode to the power-measurements of one and the same beam, nor to the power of the two beams on one and the same photodiode, it does not cancel by equation (2.3) or (2.4). Therefore, this extra-noise had to be subtracted in preparation for the analysis of TM-reflectivity.

The evolution of TM1-reflectivity is shown exemplarily in figure (2.6). The time-series was normalised to its mean, because the losses in the different beam-paths give a systematic error to the measurement.

The error-bars of the measurement represent the standard-deviation from the averaged one-minute-long power-time-series, propagated to R_{TM} with equation 2.3, normalised by mean.

Since the remaining intensity noise is very low, it is obviously not limiting the accuracy of this measurement. To estimate the impact of other possibly unknown low frequency noise sources, a reference to this measurement was computed from all power-measurements without TMs in the beam-path. The error computes to about $\pm 2 \cdot 10^{-3}$ [W/W] .

Therefore, no changes in the TM-reflectivity above this confidence interval could be

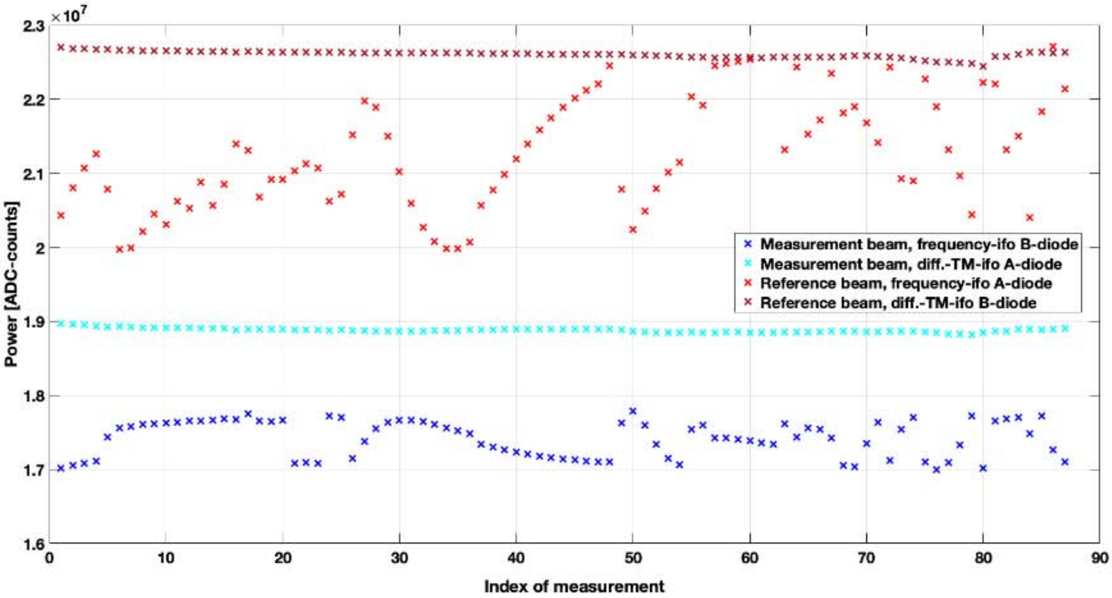

Figure 2.5: Single beam power of reference and measurement beam in selected PD-channels. Instead of time the index of measurement was chosen as x-parameter to increase the visibility (comparison with figure (2.3)).

detected during the whole LPF-mission. Additionally, in extrapolation to LISA, a stable TM-reflectivity can be expected, which means no further losses in light, no extra heat-transfer to the TM and constant radiation pressure.

2.4 PD-responsivity

As described in the nominal mission report (see [1]), the power-modulation-investigation was performed once at the beginning and once at the end of the mission. During the extension phase one more measurement was taken, so that the overall observation-duration was nearly doubled and covers more than a year.

At the end of nominal mission characterisation measurements for the power-modulation were performed, including an increase in modulation depth, a reference power modulation with the reference beam (that does not apply radiation pressure) and a counter modulation with both beams to keep the PD-temperature stable while applying radiation pressure. A change of the modulation frequency was not necessary due to the several higher harmonics.

Again, the analysis of these characterisation measurements uncovered a new unexpected effect that was only observable due to the great performance of the interferometric readout. This effect was studied in the meantime and is therefore described here although the data was assembled during nominal mission.

The DWS-signals during increase of the modulation-depth showed a correlated signal that could not be explained by real TM-motion. Several theories were developed and studied until the only valid explanation left, was an error in the processing of the phase-meter. A cross-check with the implemented data-processing architecture and other experiments with

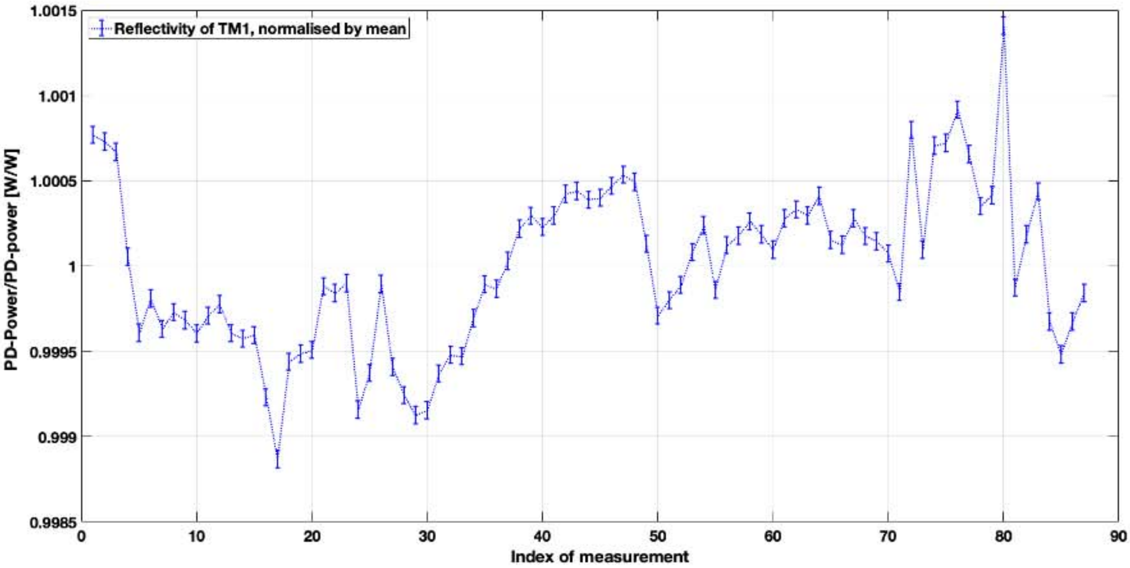

Figure 2.6: Evolution of TM1-reflectivity over the whole mission duration in dependence of the measurement-index (comparison with figure (2.3)). The grey surface shows the deviation between several reference measurements and represents the error to the TM-reflectivity measurement. There is no measurable change in TM-reflectivity over the whole mission duration

power-changes lead to the conclusion of a tiny coupling-parameter from laser-power- to phase-readout.

Nevertheless for the nominal modulation depth and of course also for the intensity noise without modulation, this effect is negligible.

Therefore, the determination of the PD-responsivity is not affected by the coupling.

Figure (2.7) shows the evolution of the virtually combined responsivity of PD12A and PD12B computed by equation (2.8). The error to the absolute parameter is higher than to the evolution during mission, due to a systematic error from the poorly known losses between TM and PD. Therefore, the computed responsivity was normalised to its mean, to show only the relevant evolution in time.

With an accuracy of about 1%, there is no change in PD-responsivity in more than a year. This further supports the applicability of the used type of photodiodes for LISA.

2.5 Polarisation

Monitoring of the single beam powers on the QPDs showed unexpectedly high noise, although the power control loop was working pretty well. The noise appears at very low frequencies, since the power during one investigation is stable, but in between several measurements the power levels are varying a lot.

Special characteristic of this noise is its appearance in the several PD channels, which showed an interesting pattern. In the end this noise distribution allowed to rule out different theories and identify the origin of the noise. The corresponding model fits the data very

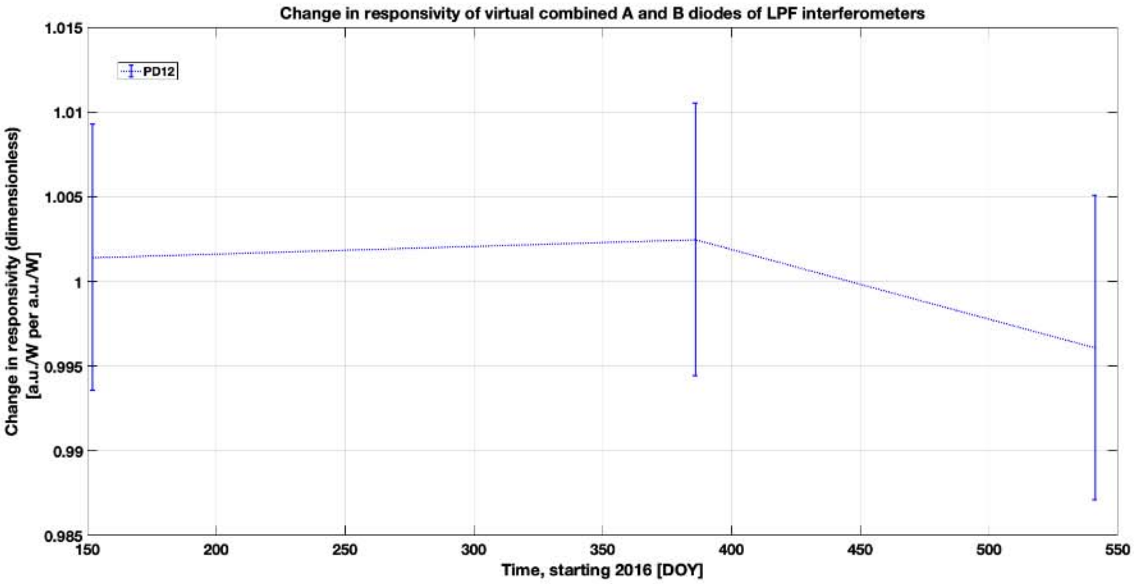

Figure 2.7: Evolution of of virtually combined responsivity of PD12A and PD12B. The last measurement was taken during mission extension.Within errors there is no change in photodiode-responsivity over the whole mission duration.

well and laboratory measurements further support the theory. In the following the special distribution of this noise is described together with analysis and results from subsequent laboratory measurements, made in this scope.

Both beams are affected by the noise, but for the reference beam it is, with up to 14% fluctuations in power, more than three times noisier than for the measurement beam, with up to 4%. With a significant Pearson correlation coefficient of -0.35 the noise is only partly negatively correlated. For most of the several QPD-measurements of the same beam the correlation is close to one. But the noise has three different levels: for the reference beam the frequency-interferometer A-diode is mostly affected by the noise. The corresponding B-diode shares the next lower level with the A-diodes of reference- and TM1-interferometer. The lowest level is shared by the B diodes of reference- and TM1-interferometer and the A-diode of the differential TM-interferometer. The B-diode of the latter one surprisingly seems to be mostly unaffected by the noise.

For the measurement-beam this pattern is equivalent with inverted A- and B-diodes. This inversion of course is the first strong hint on the origin of the noise. A relation of the noise to the PDs can immediately be ruled out, because the two beams have different effects at one and the same diode. Interfering ghost-beams could also be excluded after a detailed analysis of the OB-layout. Obviously the effect seems to be dependent on the optical properties of the recombination-BS, leading to higher noise in the transmitted beam (which is the beam on the inverted diode for the other beam). A detailed correlation-analysis, where the noise-pattern is amongst others compared to the number of the different optical coatings present on the OB further supported the theory:

→ The only fitting correlation to the noise-pattern is the number of transmissions through the 50:50-coating of the OB-BSs.

The three different power-levels then pointed in the final direction: The splitting ratio of the BSs strongly depends on polarisation. For the off-nominal polarisation the BSs transmit about 80 % of the light and therefore only reflect 20 %. This fits the separation of the power-levels very well.

For verification of the theory a model for polarisation-dependent power-distribution on the OB was developed. The model was improved step by step, so that it accounts for the power-control-loop, different BS-angles towards the beam and temperature dependent photodiode-responsivities. Results of the evaluated model together with the data for mission extensions is shown in figure (2.8).

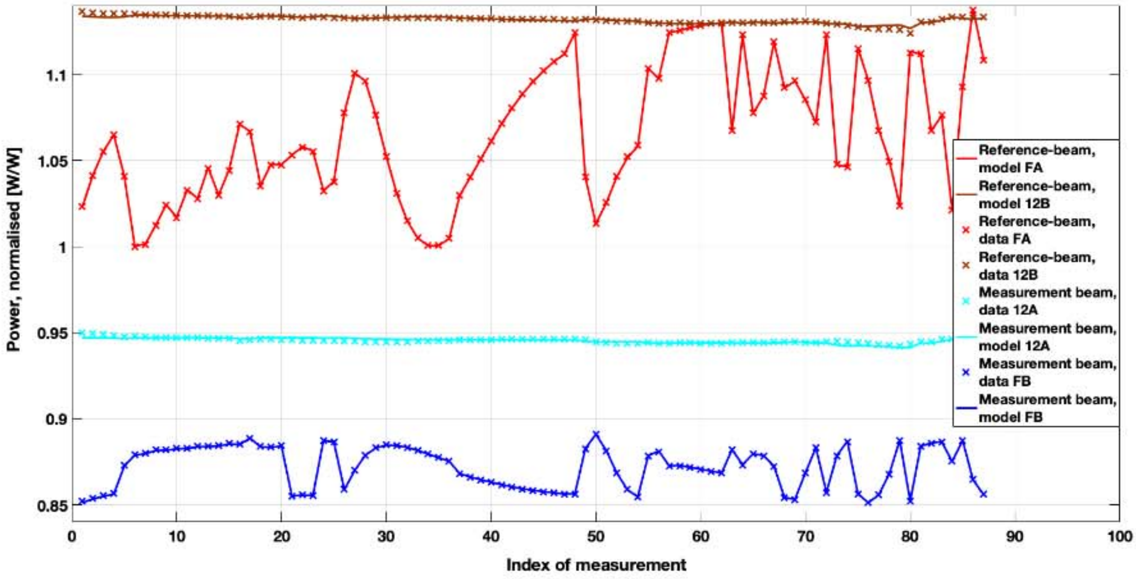

Figure 2.8: Single beam power measurements of the whole mission for selected PD-channels, together with the evaluated model of polarisation-instabilities.

It shows that the polarisation in the reference beam is up to 12.25° (corresponding to 4.5% of power with parallel polarisation to the OB) rotated to nominal polarisation. The obtained splitting ratios were supported by laboratory measurements with flight-spare hardware. Furthermore the theory could be verified by measurements with the LPF flight-spare optical bench, located in Glasgow. Here the polarisation on the OB was rotated with a polarisation filter. The resulting polarisation-angle could be retrieved from the single-beam power-measurements. Even for large offset polarisation angles of 35° the model predictions fit within one percent errors.

Using the verified model the LPF-data could be corrected for polarisation noise.

Next to the analysis of the flight data, also several investigations were undertaken, to find out about the origin of the polarisation fluctuations. Many possible mechanisms need to be rejected, such as thermally induced mechanical stress. Very recent measurements show promising results, which are still under investigation.

2.6 Impact on LPF science

The long-term monitoring of single beam-powers uncovered significant low-frequency power-noise, as described in the last section. The interferometric readout itself is not sensitive to power-noise, but on second order there are mechanisms that lead to a coupling of the noise to Δ_g.

Radiation pressure:

The first and most obvious coupling-mechanism is the force applied to the TMs by radiation pressure. The off-nominal polarised light is uncontrolled by LPFs power-control loop and therefore produces an extra-force-noise on the TMs. For estimation of the applied force, the measured power at the PDs need to be separated between the two beams and in polarisation. Then the power of the measurement beam needs to be propagated polarisation dependent to the TMs.

Since the power in off-nominal polarisation is mostly uncorrelated between the two beams, the separation of the measured power into the two beams is only possible within errors.

The resulting propagation to force can therefore only be estimated with an upper and lower limit. The correlation to the power-noise of the nominal polarised light is further unknown, wherefore again only limits for the overall combined radiation pressure could be computed.

It was found, that the power in off-nominal polarisation is dominating the radiation pressure contribution to Δ_g below 0.1 mHz. Nevertheless the contribution is still well below the observed noise at low frequencies and therefore excludes as originator of the so-called low-frequency-tail.

Balanced detection:

Another coupling-mechanism, directly correlated to the power noise is the balanced detection scheme. Balanced detection is used to reduce the coupling of relative intensity noise around the heterodyne frequency to the phase-readout. The efficiency of the reduction is dependent on differential beam-power. The observed power noise is different for the two beams and therefore impacts the efficiency of balanced detection. Fortunately the power noise on LPF is very small, so that the decrease in balanced detection is negligible.

Phase read-out error:

Besides the direct impact from power noise, described above there is another coupling-mechanism, based on the underlying effect - the polarisation-instabilities.

The measured extra-light on the OB is orthogonally polarised to the nominal beam. Therefore, it can not interfere with it. But both beams contain light with off-nominal polarisation. Therefore, these components from both beams can interfere and produce an extra heterodyne-signal, as can be seen in figure (2.9).

In the LPF-design the reference-interferometer is foreseen to allow subtraction of such path-length noise, that is not produced by real TM-motion. But the reference beam is much more affected by the power-noise than the differential-TM interferometer. Therefore, only a small amount of the extra-phase from off-nominal polarised light is removed. The implied readout-error can be computed by the phase-relation between the two heterodyne signals. Unfortunately there is no knowledge of the phase.

Since the optical properties of the OB-optics depend on polarisations the beam-paths on the OB also differ between polarisation-states. These different path-lengths result in a phase-offset between the heterodyne signals from the two orthogonal polarisation states (the nominal polarisation - S-pol and the one orthogonal to this - P-pol). A static phase-offset is not relevant for the measurement of differential acceleration. But, it is further known, that the power of the heterodyne amplitude in off-nominal polarisation changes with time. In figure (2.9) this could be expressed by the red vector changing its length. The phase computed from the sum of both vectors then also changes with time. Hence, also a static phase-offset between the two polarisations leads to a small error in the phase-readout.

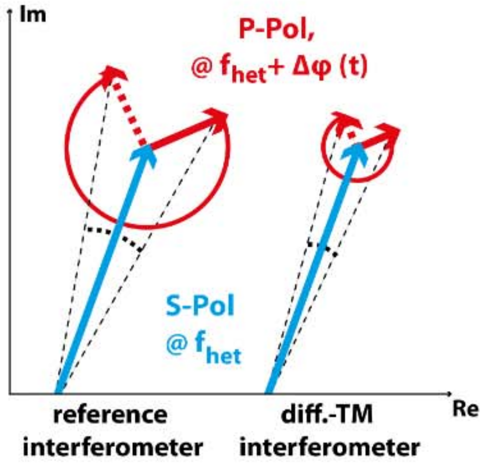

Figure 2.9: Heterodyne phase of orthogonal polarisation-states

In the actual theory of the polarisation-noise origin, it is assumed that the off-nominal polarised light arises from the optical-fibers. The path-length through a fiber heavily depends on the polarisation. Therefore, the case of a differing phase-relation between the two heterodyne-signals is more likely than a constant offset (figure (2.9): rotation of the red vector around the blue one).

With this assumption, the impact of the extra heterodyne signal gets much bigger. From the modelled power in off-nominal polarisation the maximum error of the spurious phase in differential-TM-displacement can be computed: The maximum implied displacement-error is about 200 pm. But there is no information about the frequencies of the implied noise.

Of course the impact of a displacement-error on acceleration strongly depends on the relevant frequencies (the contribution scales with the square of the relevant frequency).

For high frequencies the implied error would be huge, much bigger than the observed noise. Since the observed noise in differential acceleration in the measurement-band is well understood, a coupling at these frequencies can be excluded.

Hence, the relevant frequencies are expected to be below the measurement band.

Fortunately, for those low frequencies also the impact of 200 pm displacement-noise on Δ_g is negligibly small.

In summary the impact of the unexpected low-frequency power-noise on LPF-science was studied in more detail and no major impact on the OMS-performance could be found.

3 Laser frequency noise stabilisation and interferometer path length differences

The coupling of laser frequency noise into the phase measurement, the laser frequency control loop and the first dedicated interferometer path length difference measurement have been explained in the previous report [1].

However, let us emphasise again that the impact of the laser frequency noise on the phase measurement depends on the difference in optical path length between the measurement and the reference beam in our LISA Pathfinder (LPF) interferometers. Consequently, it was minimised in the construction processes. Any remaining difference can be found by studying the impact of laser frequency modulations onto the phase measurements as it is done in the dedicated path length mismatch experiments. Apart from reducing the impact of the laser frequency noise, the laser frequency fluctuations themselves have been suppressed by a nested control loop on LPF.

Here, we summarise again the loop characterisation experiments performed during nominal mission operations and the mission extension. In addition, we present another path length mismatch experiment performed during the mission extension.

3.1 Laser Frequency Noise Stabilisation

Including the mission extension, we have performed five laser frequency control loop measurements, as listed in Table 3.1. These measurements have been distributed over a time span of more than one year to assess the long-term stability of the performance. As for all long-term measurements, the mission extension was extremely helpful in this respect. This experiment does not rely on the LISA Technology Package (LTP) being in the nominal science mode. This way, it could also be performed at times when the test masses have been held by the caging and release system, indicated in Table 3.1 as ‘TMs grabbed’. This was the first type of measurement related to the laser frequency noise.

In addition, as a second type of measurement, we have recorded the remaining in-loop

exp number	date	satellite configuration
1	27-01-2016	TMs grabbed
2	01-06-2016	TMs drag-free
3	13-06-2016	TMs drag-free
4	22-01-2017	TMs drag-free
5	06-04-2017	TMs grabbed

Table 3.1: An overview of the fast frequency loop injections for loop performance assessment.

laser frequency noise at 10 Hz at selected times during the mission extension. During most of the quiet periods when we measured the residual acceleration, the so-called 'noise runs', the frequency noise was downloaded at 1 Hz to minimise the telemetry load.

At other occasions during the mission extension, the laser frequency control loop was deliberately deactivated to measure the laser frequency fluctuations of the free-running laser. These measurements have been confirmed from the in-loop feedback signals up to 0.5 Hz due to their limited sampling frequency of 1 Hz. This was the third type of laser frequency noise related measurements.

Our current results from these three types of measurements and noise run data can be summarised in three statements:

1. With the laser frequency stabilisation being active, the laser frequency noise was below its requirement at the investigated times of 10 Hz data. There was no systematic change in the frequency dependence of the measured laser frequency fluctuations with and without the control loop being active over the time of the mission and compared to ground tests.

2. The control loop achieved its goal and the performance did not seem to degrade. The laser frequency fluctuations could be suppressed by a factor of approximately 400 at 13 mHz.

3. We noted irregular instantaneous changes in noise behaviour as shown for example in Figure 3.1. These changes were similar to what was seen in the flight model and on-station thermal test campaigns [13][14]. This could not be explained at that time. In this regard, the in-flight data is still under investigation. We can see the impact of this behaviour in Figure 1.2 in the longitudinal measurements. Even though the LPF Optical Metrology System (OMS) performance exceeded all expectations nonetheless, this is interesting because similar lasers have been used in other space missions and are planned to be used for Laser Interferometer Space Antenna (LISA) as well. There we would like to avoid all kinds of additional noise sources possible.

3.2 Measurements of Interferometer Pathlength Differences

During the LPF mission extension, we also performed another dedicated path length mismatch experiment. The aim of this experiment was to ensure that the path length mismatch estimated is independent of the laser frequency modulation amplitude. This experiment was performed on January 22nd 2017 and the laser was frequency modulated three times with the same modulation frequency but with changing modulation amplitudes. Another modulation at a different frequency with the same modulation amplitude was added as well. The modulation time series is shown in Figure 3.2. Our current results from the path length mismatch experiments indicate that

- the change in coupling, and thus the path length mismatch, from a frequency modulation to the o12 measurement seems in agreement to expectations if we command the reference TM to an offset position and thus change the optical path length of the measurement beam (compare [1] and [15] for details);

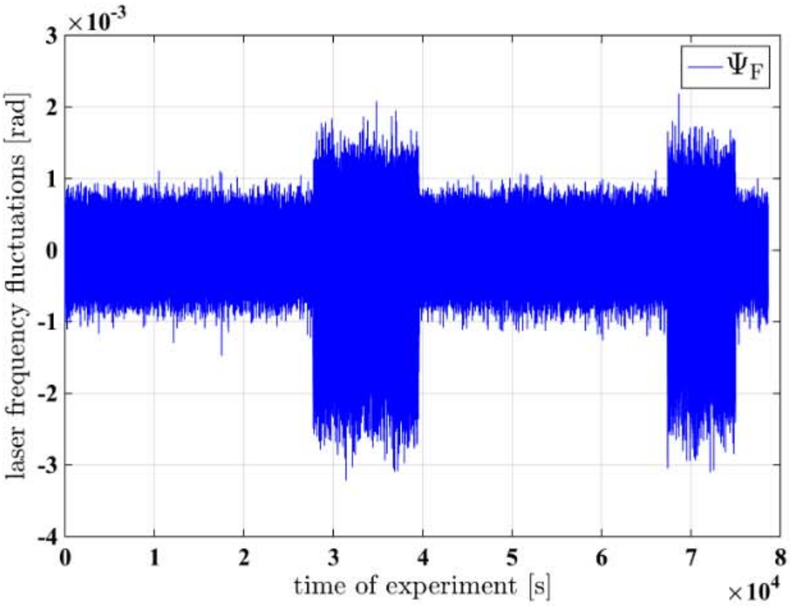

Figure 3.1: An in-loop measurement of the laser frequency noise as measured by the frequency interferometer after subtraction of the reference interferometer measurement. The data was recorded during the first ‘noise run’ which started on March 1st 2016. This is one example where irregular instantaneous changes in the noise behaviour could be observed.

- the measured path length mismatch is independent of the laser frequency modulation amplitude and frequency as expected;
- from dedicated laser frequency modulation experiments, the measured path length mismatch in X12 was measured to be in the order of hundreds of µm in June 2016. Variations of this number are under investigation as well as a small spurious coupling to other OMS channels.

3.3 Conclusion

The mission extension provided valuable data for all long-term measurements which is also true for the laser frequency noise and the stability of the control loop. Also after the mission ended, detailed analysis of the experiments have been performed, and the irregular changes in laser frequency noise behavior and spurious couplings have been investigated. A detailed report on this effort and the results will given in a future publication.

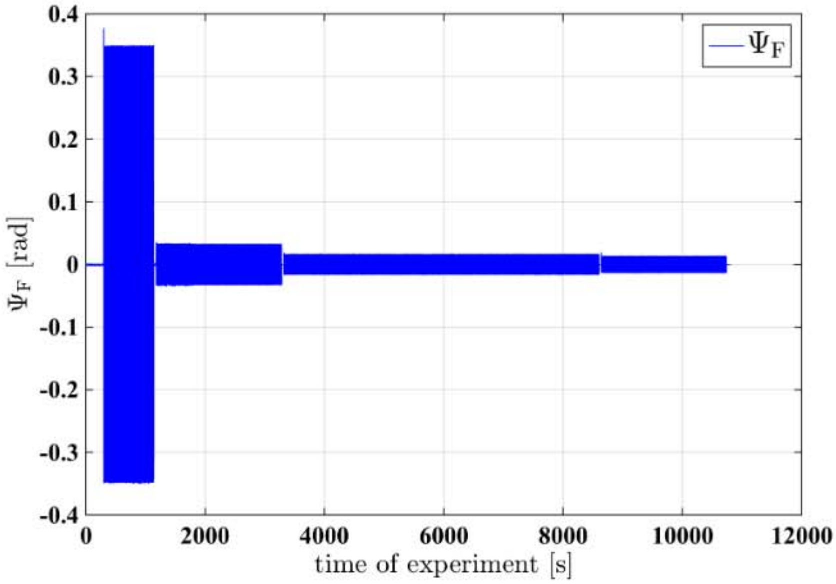

Figure 3.2: The concept of the second arm length mismatch experiment. We show the in-loop measurement of the laser frequency noise during the three modulations at 1.123 Hz with decreasing modulation amplitude and during a fourth modulation at 2.879 Hz with the second modulation amplitude of 0.05 rad. Note that as the control loop is active during the modulation, the amplitude we see depends on the transfer function of the control loop.

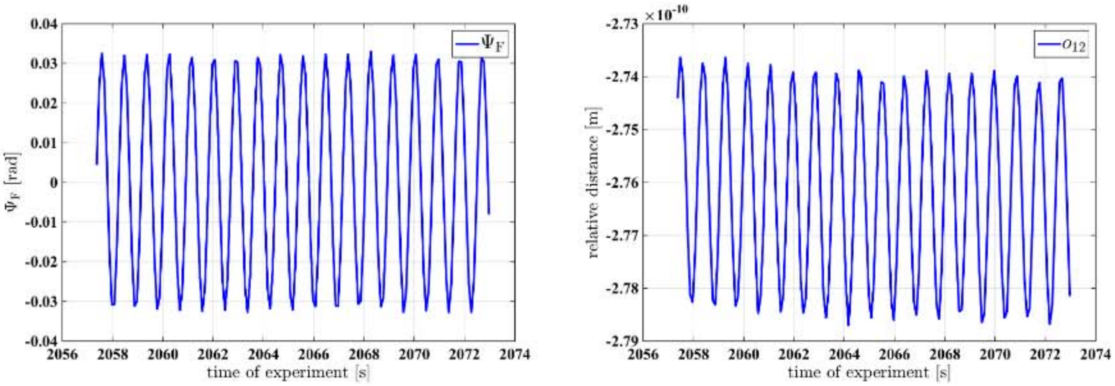

(a) frequency measurement

(b) relative distance measurement

Figure 3.3: (a): a zoom into Figure 3.2 during the second modulation. The sinusoidal modulation becomes discernible. (b): the relative distance measurement o12 during the laser frequency modulation. We compare the modulation amplitude in (b) and (a) to estimate the path length mismatch.

4 Drift mode investigation

The experiment, its goals and its first run on LPF have been explained in detail in the previous report [1]. Let us summarise the goals again:

In nominal science operation, one of the two test masses, usually called TM2, is constantly following the other TM along x. This is implemented by the so-called suspension loop. It operates outside of the LPF measurement band and uses the electrostatic actuation system to apply the required force. When estimating the residual acceleration, this force is estimated from the known commanded actuation and then subtracted. This is explained in detail in [16]. The purpose of this experiment is now to provide times without this actuation. Roughly speaking, these are the quasi parabolas shown in Figure 4.1. This has two advantages: First, prior to launch, the resulting actuation noise was expected to be limiting the LPF performance which would have been unfortunate. Here, the free-fall experiment provided a solution. In addition, during the mission, it turned out that it could provide a confirmation of the residual acceleration measured. As the actuation is switched off, this part of the calibration is not necessary for this experiment. So, if both the experiments and the analysis work as expected, the results should agree.

After the first run of this experiment in June 2016, it has been several times repeated and improved. In December 2016, the experiment ran for more than 4 days of measurement. A plot of some time series data of the differential measurement x12 is shown in Figure 4.1(a) with a zoom in Figure 4.1(b) where the quasi-parabolas become discernible. The amplitude

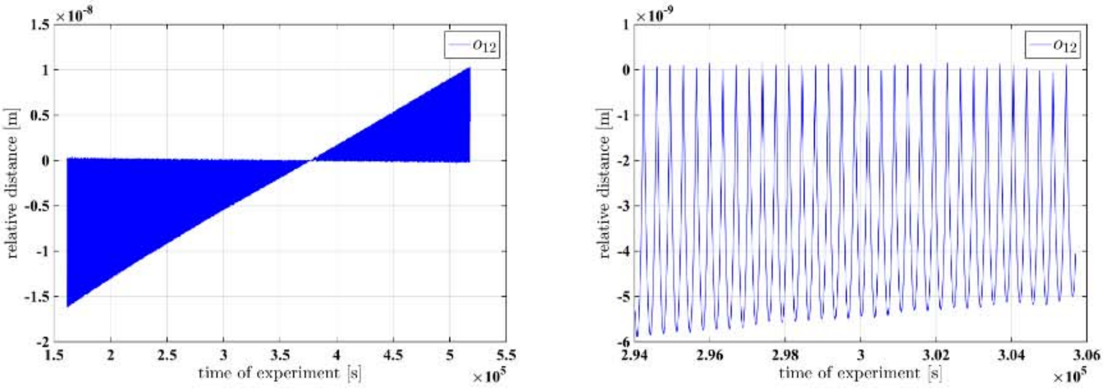

(a) measurement of relative distance

(b) zoom

Figure 4.1: (a): The measured x12 during a significant fraction the long free-fall run in the URLA configuration. The amplitude of the quasi-parabolas is changing due to changes in the local gravity field on the satellite. (b): A zoom into Figure 4.1(a). Here the quasi-parabolas become discernible.

of the quasi-parabolas is changing due to changes in the local gravity field on the satellite. In addition, a constant out-of-loop force of 11.2 pN was applied along the x-direction of TM1 [17]. Its aim was to counteract the gravitational imbalance between the TMs which causes the tiny local gravity field on the satellite. Indeed, the drift mode or free-fall experiment is designed in such a way that the cycle duration is fixed but the amplitude of each of the quasi-parabolas depends on the local forces onto the TM. Thus, to keep the quasi parabola amplitude small enough to avoid difficulties with the data recording, the correct out-of-loop force was very efficient. The orientation of the quasi parabolas changed from downwards to upwards, after around 377 ks of the experiment (see Figure 4.1(a)), as the dominant force changed. Another remarkable fact about this run of the free-fall experiment is that it could be adjusted in such a way that the High Resolution (HR) actuation mode could be used throughout to ensure a stable performance. During the flights, the actuation authority was lowered to the URLA level as during a standard measurement of residual acceleration. This measurement allowed us to compare the residual acceleration levels as mentioned before. Hence, this was a very important measurement during the mission extension because only with long measurements, we can obtain a spectrum at low frequencies with small errors. Thus, a comparison to our main measurement of residual acceleration becomes more meaningful.

Data analysis for the free-fall experiment was quite challenging. The main efforts concerning this experiment have been undertaken by our collaborators from the University of Trento to obtain the free-fall experiment results as published in [17].

Let us summarise the results here. At first, it is important to emphasize that this intermittent control scheme worked very well over long times on LPF. The control strategy here is much more complicated than during standard operations, so this is a success in itself.

As expected using the nominal actuation authority levels, the free-fall control configuration reduced the measured residual acceleration significantly, compare Figure 5 in [17]. In addition, the measured performance can be very well explained by the actuation noise models. Hence, the experiment achieved it's goal from before launch.

With the URLA actuation authority, this experiment provides an important validation of the LPF performance as independently as possible using the same hardware, see Figure 4 in [17]. The important measurements of the free-fall mode in the URLA configuration shown there have been undertaken during the mission extension.

5 Sensing Cross-Coupling

As described in the LPF final report for the German Contribution [1] as well as in [2] and discussed in [18], the cross coupling of angular and lateral motion resulted in a bulge in the 200 mHz - 20 mHz frequency band, as shown for convenience in Fig. 5.1(a), which is a reprint taken from [2]. This cross-coupling signal is mainly due to the pickup of the jitter motion of the space-craft into the sensitive interferometric channel. We have described in [1], how this cross coupling was reduced by realignment of the test masses during the so-called engineering days in March 2016, as well as by another fine-adjustment in June 2016 (see section 5.4 below). Even though this realignment reduced the amount of cross coupling - as shown in Fig. 5.1(b), the model proved repeatedly inconsistent and could not sufficiently explain the data. During the engineering days only angular adjustments had been commanded, while in June both angular and lateral adjustments were performed.

The model used to compute the June adjustments seemed to explain all data existent up to that date, proved however inconsistent with the data after the lateral adjustment performed in June. This indicated that the underlying physical processes combine non-linearly, an effect that our previous model was unable to predict. It was therefore decided to perform a dedicated crosstalk experiment during the mission extension, with the aim of investigating cross-couplings from all degrees of freedom (DOF). We designed the experiment to first study the cross-coupling effects from each individual DOF, and gradually add more complexity

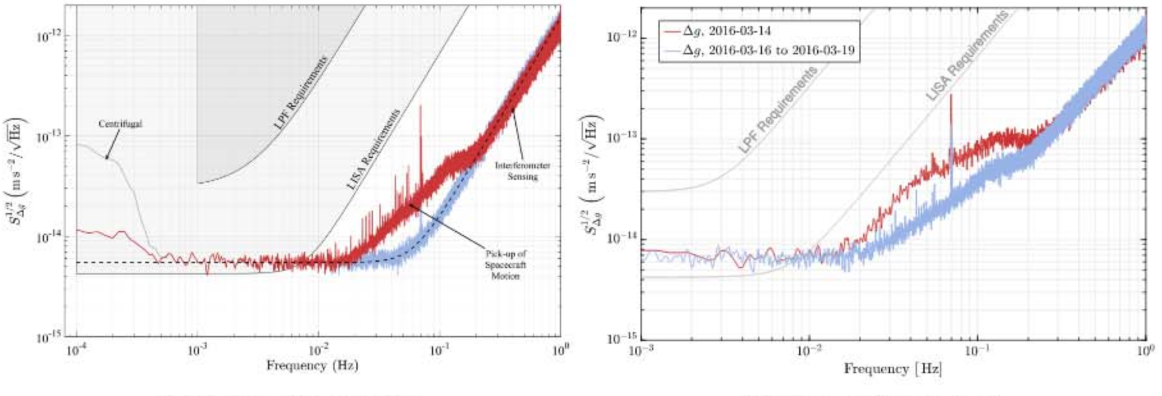

(a) Subtraction method

(b) Suppression method

Figure 5.1: (a): Result taken from [2], showing that the bulge at 200-20 mHz can be subtracted. (b) In this figure, no subtraction was performed. Instead the reduction was achieved by a realignment of the test masses prior to the second noise run.[1]

---

[1] Please note: the slight difference in curvature around 3 mHz in the LPF requirements in the two figures results from different notations: while in Fig. 5.1(a) correlated noise sources were assumed, we chose in Fig. 5.1(b) the notation for uncorrelated noise sources.

injection type	amplitude	frequency	duration	ramp duration	wait time
$y_1 = y_2$	0.5 µm	17 mHz	30 min	8 min	5 min
$y_1 = -y_2$	0.5 µm	12 mHz	30 min	8 min	5 min
y_1, y_2	0.3 µm	10 mHz, 17 mHz	50 min	8 min	10 min
$z_1 = z_2$	0.5 µm	5 mHz	50 min	8 min	5 min
$z_1 = -z_2$	0.5 µm	8 mHz	30 min	8 min	5 min
z_1, z_2	0.3 µm	5 mHz, 8 mHz	50 min	5 min	-

Table 5.1: Description of the short crosstalk experiment, describing the sequence of performed injections.

by incrementally adding more DOFs. This design allowed us to disentangle the correlated parameters of our geometrical model, and study in detail the non-linearity of the system. The resulting experiment plan had a duration of almost two days and involved sinusoidal signal injections at various frequencies. A shorter (in duration) version of this planed experiment was performed first as a test.

5.1 The Short Cross Talk Experiment

The short cross talk experiment consisted of a subset of the commands and injections performed during the long cross talk experiment. It was performed on DOY020 2017, i.e. on January 20, 2017, and lasted for 5 hours. As shown in Table 5.1, it consisted of simple sinusoidal injections to the lateral DOF of both test masses at just one 'set-point'. The experiment started with half an hour simultaneous sinusoidal injection to the lateral displacements of the test masses ($y_1 = y_2$). The injection was initially ramped-in within 8 min and likewise ramped-out within 8 min. After the fadeout was completed, 5 minutes of waiting time were defined to allow the system to fully return to its nominal state. Then, the next injection (second line in Table 5.1) was performed, where the sinusoidal injections to the test masses were defined out of phase, resulting in a counter-motion which effectively resulted in a S/C angular injection. After the rampout of this injection and another 5 minutes of waiting time, the third set of injections was performed (third line in Table 5.1), where the sinusoidal injections to the two test masses were performed at different frequencies: while y_1 was driven by a 10 mHz injection, the injection to y_2 was performed at 17 mHz. After these injections were ramped out, a comparable sequence of injections was performed to the vertical test mass degrees of freedom (lines 4 to 6 in Table 5.1). The experiments on the z-plane were similar to those on the y-plane and deviated mainly in the choice of injection frequencies. These were chosen according to the different response of the controllers along the $y - \phi$, and $z - \eta$ planes. In particular, the experimental design was chosen for the follwoing reasons. First, in order to disentangle the various cross-coupling contributions to $\Delta g(t)$ we needed to have at least three reference points across the spectrum. Secondly, the analysis of the data would become simpler and more straightforward, by taking into account the non-overlapping harmonics present in the data-stream. Finally, the amplitudes and frequencies where carefully selected in order to avoid non-linear, or irregular response of the controllers.

#	Start time (month.day	End time hour.minutes)	Set-point (Relative to initial)
1	02.04 22:02	02.05 00:08	y_1: -30μm
2	02.05 00:36	02.05 03:34	z_2: 10μm
3	02.05 04:00	02.05 07:00	z_1: 21.6μm
4	02.05 07:27	02.05 09:34	y_2: -22μm
5	02.05 10:00	02.05 13:00	η_1: 12.1μrad
6	02.05 13:25	02.05 15:25	ϕ_2: 20μrad
7	02.05 16:00	02.05 18:11	ϕ_1: 30μrad
8	02.05 18:35	02.05 21:34	η_2: -20.3μrad
9	02.05 22:05	02.06 03:27	y_1: -10μm, z_1: 5μm
10	02.06 04:32	02.06 09:35	y_1: -20μm, y_2: -10μm, z_1: 15μm, z_2: 5μm
11	02.06 10:03	02.06 15:34	y_1: -25μm, y_2: -15μm, z_1: 20μm, z_2: 15μm, ϕ_1: 10μrad, η_1: 5μrad
12	02.06 16:00	02.06 21:35	y_1: -35μm, y_2: -25μm, z_1: 25μm, z_2: 25μm, ϕ_1: 20μrad, η_1: 10μrad, ϕ_2: 10μrad, η_2: -5μrad

Table 5.2: Table representing the timeline of the long cross-talk experiment that was performed during the mission extension period, in 2017. Times are given in UTC. The shown set-points were commanded relative to their initial position (see Table 5.3).

In more general, these injections were defined in order to retrieve maximum information out of the system and tested the cross talk behavior in the near vicinity of a given system alignment. Since the cross-talk behavior significantly depends on this system alignment, it was necessary to test for different alignment parameters, which was done in the long cross talk experiment, described below.

5.2 The Long Cross Talk Experiment

The so called "Long Cross Talk Experiment" had a duration of approximately 48 hours and was performed between Feb. 04 and Feb. 06. It consists essentially of a series of short cross talk experiments (see previous section 5.1) performed at different set-points of the various DOF. We define as set-point a positional or rotational offset applied to each DOF of each of the test-masses before injecting the sinusoidal signals. In Table 5.2 the detailed timeline of the experiment is presented, together with the set-points commanded on the different degrees of freedom. Figures 5.2(a) and 5.2(b) show both the commanded offsets as well as the performed injections for the $y - \phi$ and the $z - \eta$ plane respectively.

5.3 Implications for LISA

Crosstalk between angular and lateral jitter will also be a considerable noise source in LISA. Though LISA will be designed to suppress cross talk, there will be residual cross talk in flight and experiments comparable to those described here, might be needed to characterize the cross talk and to further minimize it in flight.

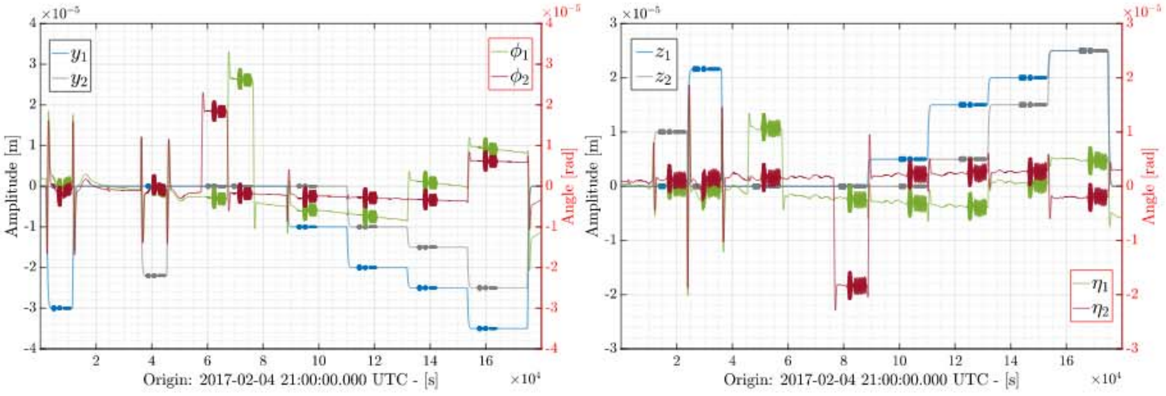

(a) Horizontal readout

(b) Vertical readout

Figure 5.2: Readout signals for test mass motion during the long cross talk experiment. All angular readout is taken from DWS signals, while the lateral degrees of freedom (DOF) are GRS readout signals.

5.4 Test mass set-points during the entire mission duration

The amount of cross talk depended on the precise position and orientation of the test masses, as described in [1, 18]. During the engineering days (see [1, 18]), and after detailed analysis of the engineering days data about three months later, the test masses were realigned. These set-points altered the amount of cross talk, but potentially also effected other experiments. The set-points are listed in Table 5.3. There was no additional realignment performed after the short and long crosstalk experiments described in this report, such that Table 5.3 defines the only realignment of the TMs performed for crosstalk reduction during the entire mission.

Parameter	standard description [unit]	DOY 076 (16.03.2016 14:28)	DOY171 (19.6.2016 8:20)	DOY177 (25.6.16 8:0)
ADP72125	x1 [µm]	0.0	0.0	0.0
ADP72126	eta1 [µrad]	**-3.5**	**-2.14**	**-2.1**
ADP72127	phi1 [µrad]	**-59.25**	**-56.32**	**-57.32**
ADP72128	dx [µm]	0.0	0.0	0.0
ADP72129	eta2 [µrad]	**3.5**	**10.3**	10.3
ADP72130	phi2 [µrad]	**-21.35**	**-33.01**	-33.01
ADP72101	x1 WR [µm]	4.799	4.799	4.799
ADP72102	y1 WR [µm]	5.742	73.7	73,7
ADP72103	z1 WR [µm]	8.749	-3.2	-3.1
ADP72104	theta1 WR [µrad]	9.26	9.26	9.26
ADP72105	eta1 WR [µrad]	-736.6	-735.24	-738
ADP72106	phi1 WR [µrad]	17.4	19.33	15.454
ADP72107	x1 HR [µm]	-0.2491	-0.2491	-0.2491
ADP72108	y1 HR [µm]	0.36	**68.36**	68.36
ADP72109	z1 HR [µm]	0.4107	**-11.6**	-11.6
ADP72110	theta1 HR [µrad]	-4.448	-4.448	-4.448
ADP72111	eta1 HR [µrad]	-742.5	-741.14	-741.14
ADP72112	phi1 HR [µrad]	-2.25	-0.32	-0.32
ADP72113	x2 WR [µm]	5.631	5.631	5.631
ADP72114	y2 WR [µm]	5.648	49.7	49.8
ADP72115	z2 WR [µm]	9.167	-10.4	28.5
ADP72116	theta2 WR [µrad]	-10.66	-10.66	-10.66
ADP72117	eta2 WR [µrad]	-173.9	-167.1	-180.7
ADP72118	phi2 WR [µrad]	554.71	543.05	566.36
ADP72119	x2 HR [µm]	0.3915	0.3915	0.3915
ADP72120	y2 HR [µm]	0.6999	**44.7**	44.7
ADP72121	z2 HR [µm]	0.7767	**-18.73**	-18.73
ADP72122	theta2 HR [µrad]	2.446	2.446	2.446
ADP72123	eta2 HR [µrad]	-188.5	-181.7	-181.17
ADP72124	phi2 HR [µrad]	598.65	586.99	586.99

Table 5.3: Changes of the test mass set points in order to optimize the cross talk suppression. Times are given in UTC. The first six lines describe offsets commanded as calibration of the interferometer readout signals, all remaining lines define offsets in the inertial sensor calibration. Numbers in bold font indicate primary changes of set points.

6 Relative Intensity Noise and longitudinal TM offsets

6.1 Introduction

The previous report already describes parts of the RIN experiments, with focus on the first experiment performed during the nominal mission. This report describes the second experiment which was performed during the mission extension. As this is a continuation of the previous text a longer introduction can be found in the previous report [1].

RIN is a property of the laser, and these intensity fluctuations are frequency dependant. From a theoretical analysis it was found that the coupling of RIN to the phase measurement of the measurement interferometers is dependant on the phase difference between the measurement interferometer signal and the reference interferometer signal.

The phase between the measurement and reference signals changes when the test mass is moved, and we see an increase in noise at high frequencies if the test mass is moved from its nominal position.

The derivation of this dependency will be published in a future paper.

6.2 Experiments

In this analysis we look at properties of the optical readout, all the analysis is performed in displacement, the units we use are [fm] and $\left[\frac{\mathrm{fm}}{\sqrt{\mathrm{Hz}}}\right]$. Most other LPF data analysis concerns forces on the test mass, and is therefore performed in the acceleration domain, with the units $\left[\frac{\mathrm{fm}}{\mathrm{s}}^2\right]$ and $\left[\frac{\mathrm{fm}}{\mathrm{s}^2\sqrt{\mathrm{Hz}}}\right]$.

Two dedicated experiments were performed to measure the coupling of relative intensity noise to the length measurement. The aim of the first one was to confirm the theoretical noise-over-position behaviour for the flight optical metrology system, since balanced detection is on it is expected that RIN at $1\mathrm{f}_{\mathrm{het}}$ is removed from the signal, but RIN at $2\mathrm{f}_{\mathrm{het}}$ should still be present.

In the second experiment, balanced detection is switched off, and the subtraction properties of $1\mathrm{f}_{\mathrm{het}}$ RIN are measured. This experiment was designed with the results of the first experiment and was performed during the mission extension.

In preparation for the mission, similar experiments were performed with an engineering model of optical bench in the laboratory at the AEI in Hannover. Due to the more noisy ground setup, additional RIN had to be fed into the measurement so that the effect was visible over the other noise sources. These lab experiments confirmed there was something worth investigating, and these initial experiments helped to design a flight experiment.

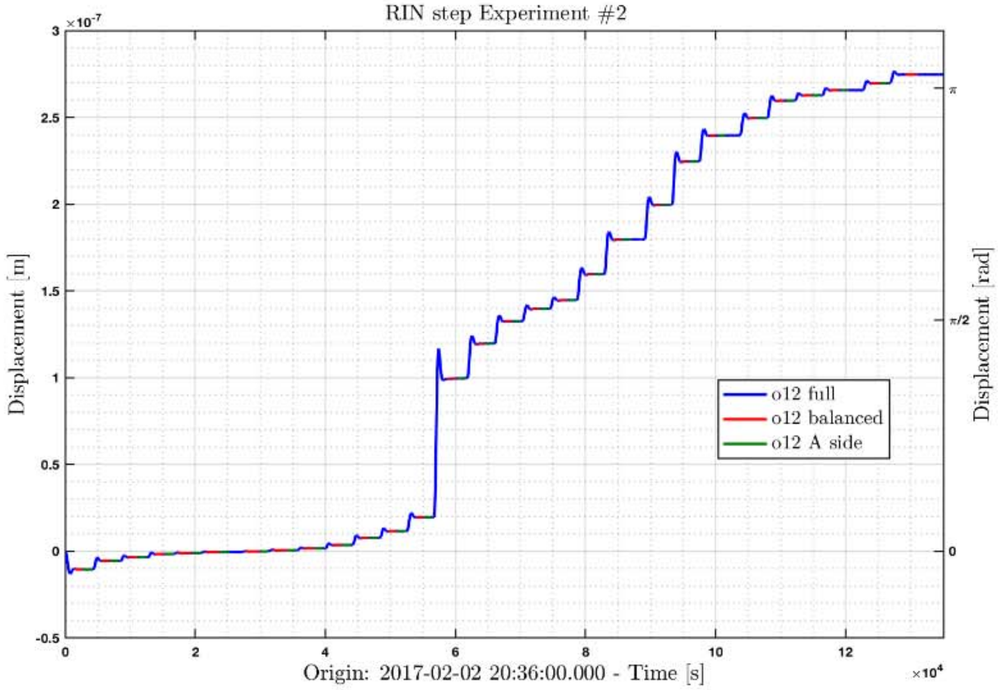

Figure 6.1: The time series of the second step experiment, plotted in blue. At each step we select a quiet timespan, shown in red with balanced detection and in green without. A closer look at one of the steps can be found in Figure 6.2. The uncertainty on the test mass position in later calculations comes from the drift during each step, the measurement error is small compared to the range of test mass offsets.

The experiments are very simple, the test mass was moved to a number of offsets from its nominal zero-phase difference between measurement signal and reference signal, the nominal test mass position corresponds to a test mass position of 0 nm.
At each offset position we performed a noise measurement. The limiting factor in this experiment is the time it takes the test mass to move to the new offset and stabilise, relative to most other experiments the test mass moves far distances of tens of nanometers per step. The noise measurement at each step should be short enough to have a reasonable number of steps, but long enough to have enough averages to calculate the noise between 0.4 Hz and 5 Hz with a reasonable error. See Figure 6.1 for the time series of the second step experiment, performed during the mission extension.

In the first experiment the test mass was moved over a large parameter space to confirm the predicted noise shape, with steps of 10 nm or 30 nm the test mass is moved from -270 nm to 790 nm, which corresponds to phase differences between the signals between $-\pi$ to almost 3π. In this experiment the noise over position measured fits to the prediction made for the coupling of relative intensity noise at two times the heterodyne frequency. This was expected because RIN at $1f_{\text{het}}$ is subtracted with balanced detection.

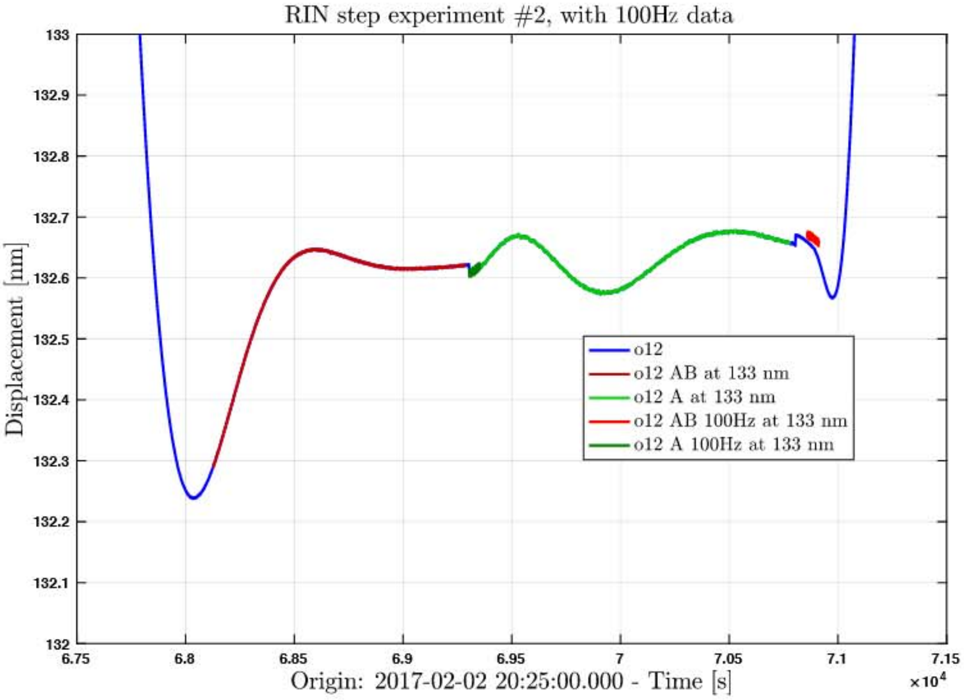

Figure 6.2: An example step of the second step experiment. The timespan where balanced detection is on is shown in red, the shorter timespan in red is recorded at 100 Hz. Balanced detection is off in the green segments, the shorter dark green timespan is recorded at 100 Hz.

In the second experiment the focus is more on the coupling of RIN near the optimal positions, this version has a smaller total range since the shape itself was established but more offset positions with smaller step sizes.

Additionally for each step balanced detection is turned off for 25 minutes, RIN at the heterodyne frequency is no longer removed from the signal in this timespan. This allows a direct comparison of the noise for the two settings for many test mass offsets. This setup aims to decouple the noise level of RIN at the heterodyne frequency, two times the heterodyne frequency, and the noise floor of ADC noise, electronic noise and shot noise. For some test mass offsets the $o12$, Ψ_R and Ψ_F signal is recorded at 100 Hz to further explain the noise behaviour at high frequencies.

Shown in figure 6.2 is an example step with balanced and unbalanced detection and 100 Hz data, the test mass offset is 133 nm, which corresponds to a phase difference of $\frac{\pi}{2}$ between measurement and reference signal. Due to the high data rate of 100 Hz, the timespan is very short.

At every position the noise spectrum is calculated, and we take the mean value of this noise spectrum over different frequency bands. This band is selected to exclude the spikes at 1, 2, 3, and 4 Hz and the rising noise towards lower frequencies, see figure 6.3 for a selection of spectra with balanced detection, and figure 6.4 for A diode spectra.

The offsets were selected to investigate around zero test mass offset, around maximum

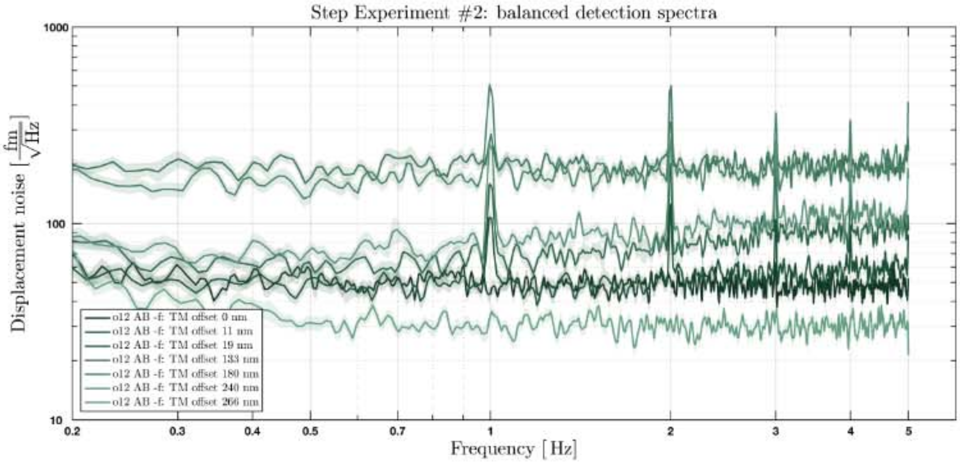

Figure 6.3: Example spectra for test mass offsets between 0 nm and 266 nm, the spectra were calculated with 300 samples in each fft with an overlap of 50% and an Hanning window. These measurements were taken with balanced detection on.

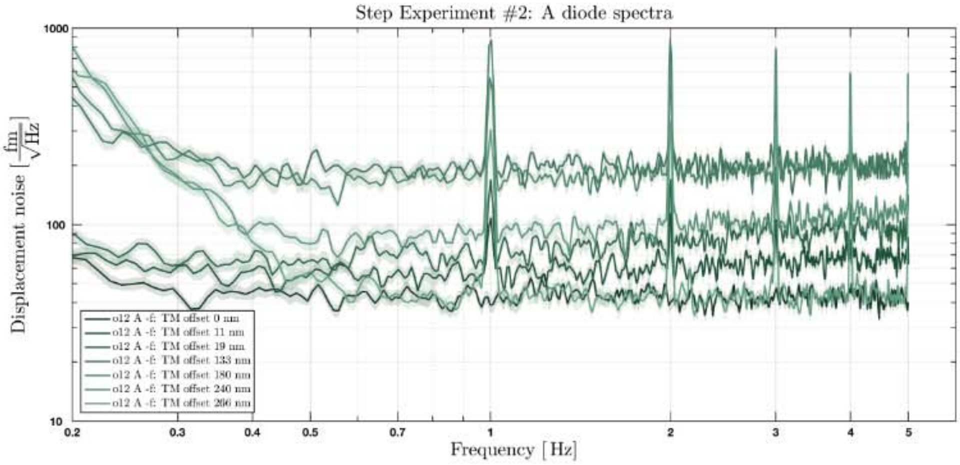

Figure 6.4: Example spectra for test mass offsets between 0 nm and 266 nm, the spectra were calculated with 300 samples in each fft with an overlap of 50% and an Hanning window. These measurements were taken with only the A diodes.

noise and around the first noise minimum, the plotted spectra therefore are around the lowest and highest noise levels.
The noise level near zero test mass offset is higher than expected due to other noise sources present at the start of the experiment, the expectation for balanced detection is to have a similar noise level for offsets of 0 nm and 266 nm. For a single diode the noise level of 266 nm offset should be higher than 0 nm due to the $1\mathrm{f}_{\mathrm{het}}$ RIN contribution.
The analysis of this experiment is still ongoing.

An example of high frequency data can be seen in Figure 6.5 with an offset of 133 nm and Figure 6.6 with an offset of 240 nm, for both balanced detection and the A diode measurement.

The lines at n Hz which are common in the 10 Hz data can also be found in the 100 Hz data, the noise level in this range is similar between both sampling frequencies. Except for the balanced measurement in Figure 6.6, the noise increase at 10 Hz in the 100 Hz data aliases down and leads to the increase of noise above 2 Hz.

The source of this 10 Hz noise is still under investigation, but it might explain varying noise sensing noise levels and non-white noise shapes.

The results of this experiment were compared to the noise at different test mass positions from other experiments, namely the free fall experiment, but also for small test mass motions during noise runs. The noise shape of this dedicated experiment is consistent in the position behaviour to the other experiments. The amplitude of the noise changes with the status of the laser and is different for each experiment.

Due to a scheduling conflict with the cool down of the satellite before the start of the timeline, the second experiment did not run as planned. The timeline is cut short, and the temperature was not yet stable at the beginning of the experiment, which lead to an increase in noise. This noise is removed by balanced detection during normal operations, enabled by the presence of the redundant PDs on both beamsplitter ports.

An interferometer without this subtraction or a random phase offset for each experiment would show a wildly varying noise level at higher frequencies over the course of the mission, and certainly make it harder to reduce the overall noise in a controlled manner.

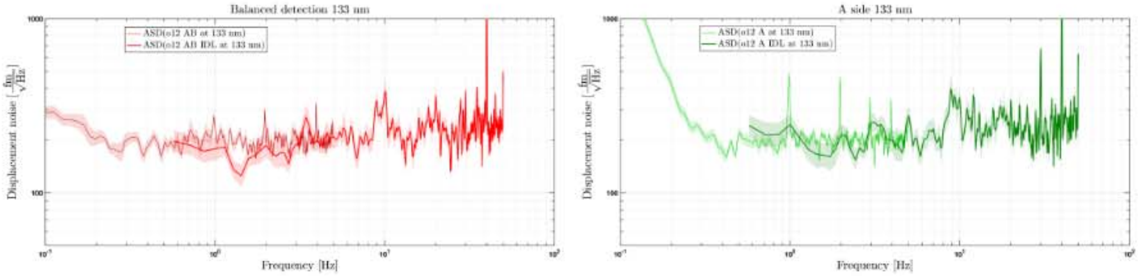

Figure 6.5: In red is the measurement with balanced detection on, both 10 Hz data and 100 Hz data. Shown in green is the measurement with balanced detection off, also with 10 Hz and 100 Hz. These spectra were measured with a test mass offset of 133 nm, at the maximum noise level expected for $2f_{het}$ RIN. The spectra were calculated with 700 samples in each fft with an overlap of 50% and BH92 window.

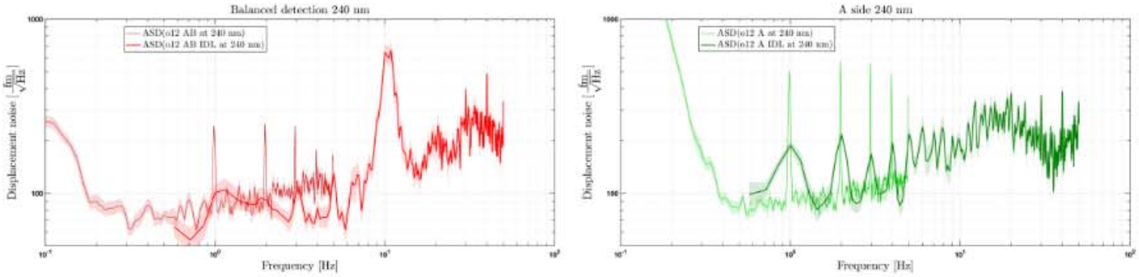

Figure 6.6: In red is the measurement with balanced detection on, both 10 Hz data and 100 Hz data. Shown in green is the measurement with balanced detection off, also with 10 Hz and 100 Hz. These spectra were measured with a test mass offset of 240 nm, this offset was chosen to show aliasing from a noise peak around 10 Hz down to the sensing noise floor in the 10 Hz data. The spectra were calculated with 700 samples in each fft with an overlap of 50% and BH92 window.

6.3 Noise over position

For both step experiments the noise over position is calculated, in both cases for the frequency band between 0.55 Hz and 0.9 Hz. The distribution of steps is different, and since the experiments were performed almost a year apart the amplitude of RIN is expected to be different, but the general behaviour should be the same. This is found to be true for the experiments performed, the noise shape follows the theoretically predicted behaviour for $2f_{het}$.

The amplitude of the noise is different between the two experiments because they were perfomed almost a year apart and the laser was in a different state.

We're interested in the subtraction of $1f_{het}$ RIN, and if only the measurement interferometer had one diode turned off then only in this signal $1f_{het}$ RIN would be present, and the reference signal would not have the same noise to subtract in the calculation of $o12 = x12 - xR$.

In the measurement with only the A diodes the fit result of the balanced case for $2f_{het}$

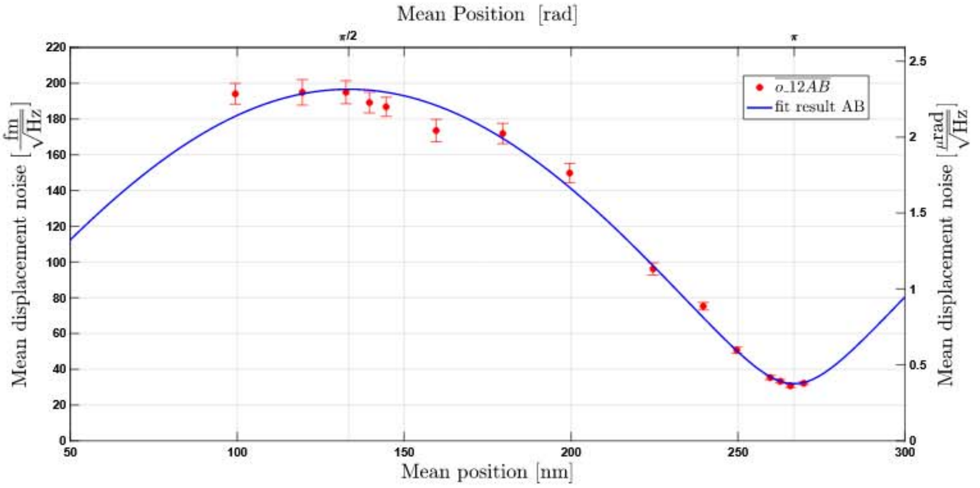

Figure 6.7: This plot shows the noise over position of second step experiment, the mean test mass offset is shown in [nm] as well as in [rad]. The mean noise level is calculated in $\left[\frac{\text{fm}}{\sqrt{(\text{Hz})}}\right]$ as well as in $\left[\frac{\text{rad}}{\sqrt{(\text{Hz})}}\right]$. The measured mean noise level with balanced detection is shown in red, the first points of this experiment were removed because the laser was not in a stable state. The fit result for experiment, plotted in blue, is included, the noise over position is consistent with 2f_{het} RIN.

RIN is used to seperate the 1f_{het} RIN, due to additional noise problems during the start of the experiment the analysis of this second part of the experiment is still ongoing.
A preliminary plot can be found in Figure 6.7, this splot shows the noise over position of the balanced detection measurement of the second step experiment, with a first fit to the data.

These results are preliminary and an improved version will be published in a future paper.

From the results of the step experiment performed during mission extension we can see that the high frequency noise level does not increase by much if balanced detection is off, as long as the subtraction with the reference phase still works.

This is good for redundancy, even if one of the photodiodes in LPF had failed, or on LISA, would fail there is still a way to measure with high accuracy from the perspective of RIN, and the other noise present during the start of the experiment.

With a comparison between the first and second step experiment, as well as the RIN DWS experiments in section 7, we can see that the RIN level changes with time.

Due to the limited number of experiments the cause could not be found, but it would not be unreasonable to expect changes in the laser performance under different operating conditions.
During normal operational conditions, with the test mass near the interferometric zero, this RIN noise does not have a relevant impact on the performance.

This can be seen as a big success of the investigations into this effect before and during LPF Operations.
The results of these experiments will help with noise projections on LISA, and with the

efforts to reduce the impact of this test mass position dependant noise.
Future research will include the coupling of RIN through the TDI algorithm.

6.4 RIN direct measurement

This experiment was performed during the last days of the mission extension. For this measurement one beam is turned off, which allows to measure the intensity fluctuations directly. Since there is no heterodyne signal the phasemeter transfers the fluctuations at or near the f_{het} down into the measurement band. The phase signal measured like this is caused by RIN near $1f_{het}$, to measure the RIN near $2f_{het}$ in the same way the heterodyne frequency was set to 2kHz.

The analysis of this experiment is still ongoing, the scaling from the measured phase signal in meter [m] back to relative intensity fluctuations is not immediately obvious.

7 Experiments regarding DWS

7.1 An improved DWS step experiment in the mission extension

During the main mission, an experiment was performed to assess the DWS noise behaviour for varying test mass two angles. The procedure allowed a very specific investigation that led to an improved understanding of RIN coupling from twice the heterodyne frequency. The details about this experiment can be found in the report about the main mission [1].

During the mission extension a refined version of the DWS experiment was planned.[1] A few shortcomings of the previous version were:

- A better RIN model verification needs to be based on larger electronic phase shifts. With the previous investigation important model parameters such as the maximum amplitude and the sinusoidal shape could not be confirmed by the measurement alone, but instead only for the case of a linearised model for small angular offsets.
- In LISA, imaging optics will avoid beam walk effects on the measurement photodiodes. In the first DWS step experiment beam walk is not suppressed. This is only a few percent of the beam radius but it is expected to cause an additional drop in contrast. Transferring the result to LISA is more robust if the beam walk is kept close to zero.
- The model predicts RIN coupling from both the heterodyne frequency and its second harmonic. However, since the OMS utilizes the so called balanced detection scheme to minimize common mode additive noise components, the RIN noise coupled from the heterodyne frequency is expected to be subtracted by design. An unbalanced detection mode is expected to show both noise components.
- To investigate the effect of the 2nd moving average filter aboard LPF in the high frequency range a set of data from before that step can be requested through the IDL mechanism aboard the spacecraft.

The goals of this experiment were:

- An improved measurement of the RIN noise slope for the balanced and unbalanced detection case without beam walk effects for test mass two.
- Assess the DWS noise performance for test mass one. Its contributions can be characterized analogously.
- A better (RIN) noise model verification and, if needed, readjustment.
- Characterization of aliasing due to maximal decimation in the phasemeter.

---

[1] The following content is based on [19].

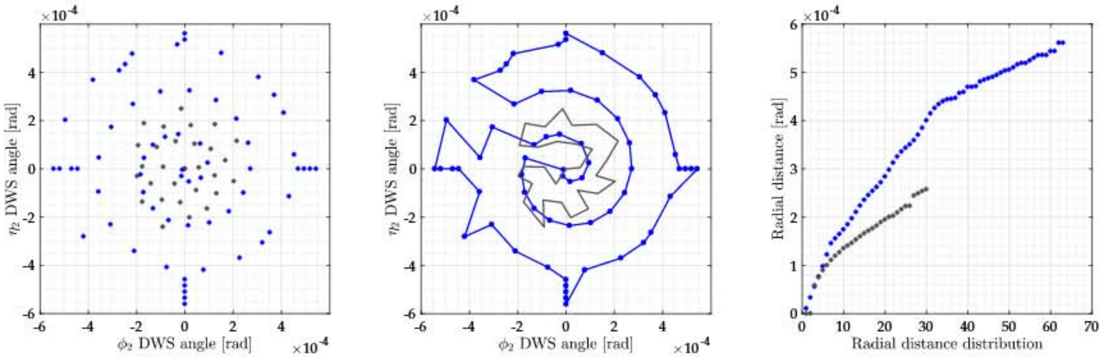

Figure 7.1: Parameter space during the second DWS step experiment. In blue are the planned set points, the first experiment is shown in black. Note that test mass one were commanded by factor 0.27 of the test mass two slews. In comparison to the first run more than twice as many points were used and they are placed at larger radii. For the first experiment generic random sampling of the parameter space has been used, whereas now the points were chosen to follow a spiral distribution.

- Estimation of the DWS noise contribution in a comparable LISA setup.

The data from this experiment were expected to be also usable for the contrast model and the GRS calibration for cases of simultaneous phase shifts. During the tilts it could also be possible to characterize the controllers by looking at the test mass trajectory dynamics.

7.1.1 Investigation design

The principal design was similar to the original approach and can be seen in Figure 7.1. Differences from the first experiment are larger tilts and a corresponding actuation scheme for test mass one to compensate beam walk. The specifically requested measurement parameters in this experiment were the DWS signals

$$\eta_i^{\mathbf{DWS}} \quad \text{and} \quad \phi_i^{\mathbf{DWS}}, \quad i \in \{1, 2\},$$

which were available with a sampling frequency of 10 Hz and the corresponding contrast signals

$$c_i, \quad i \in \{1, 12\},$$

with a sampling frequency of 1 Hz. Obviously the 10 Hz data package was required for the noise floor analysis around 1 Hz to 5 Hz, but for modelling the contrast such high frequency components were not expected to have a big impact. Nonetheless, a large drop in contrast was considered due to the large tilts. To meet satellite safety requirements for the new design a number of pre-investigations were run. They included sinusoidal injections up to 600 μrad simultaneously in both test masses, single slews up to 1 mrad and a test of the proposed beam walk compensation scheme (see below). Measuring without balanced detection implied to mask one side of the DMU which might have caused transients due to the rapid loss of signal in the processing and control units.

Test mass	Photodiode	Distance [mm]
TM1	PD1A	301.885
TM1	PD1B	289.186
TM1	PD12A	492.715
TM1	PD12B	504.493
TM2	PD12A	128.917
TM2	PD12B	140.694

Table 7.1: Lever arms between the test masses and the respective object. They represent the accumulated optical path lengths of the beams. Interestingly, the distances between the DMU PD12A and PD12B side photodiodes differ by 11.8 mm making it impossible to completely cancel beam walk. The values listed here were used for the lever arm calculations and are provided by the author of [20].

Data analysis showed that the time between specific set points should have been increased to enhance the data quality by allowing more time for the test mass to settle at each set point. Unfortunately, there was no option during the mission extension to re-run this experiment another time. The reason for this behaviour is unknown, as the estimated time to stabilize was calculated from the previous experiment and appears to have changed.

7.1.2 Compensating beam walk

The actuation scheme was based on the following linearised geometrical model. We use the optical lever arms within the OMS given in table 7.1. These were derived from an optical model (see [20] for a description of the model) implemented using the software library IfoCAD [21]. It has to be noted that the distance from TM2 to the two measurement photodiodes PD12A and PD12B, which are used for balanced detection, is not the same. They differ by 11.8 mm. In general there were two intertwined geometrical couplings modulating the beam walk. The main effect is the lever arm (times angle) effect itself, whereas the second effect arose from the change of the lever arm due to test mass rotation: Tilting around the center of mass caused a piston effect which changed the relative distance. This second effect was neglected in our compensation procedure because the lever arms were large compared to the reduction coming from the piston, and because the two photodiodes did not have equal geometrical distance to the test masses, making it impossible to completely compensate the effect.

7.1.3 Piston effect

The piston effect was approximated by two components, one is the linear piston effect which arises when the light is not exactly incident with a line through the test mass center and a second one giving a quadratic order contribution, describing tilts around the point of reflection.

$$x \approx \underbrace{d\phi}_{\text{Linear piston effect}} + \underbrace{\frac{s}{2}\phi^2}_{\text{Quadratic piston effect}}. \tag{7.1}$$

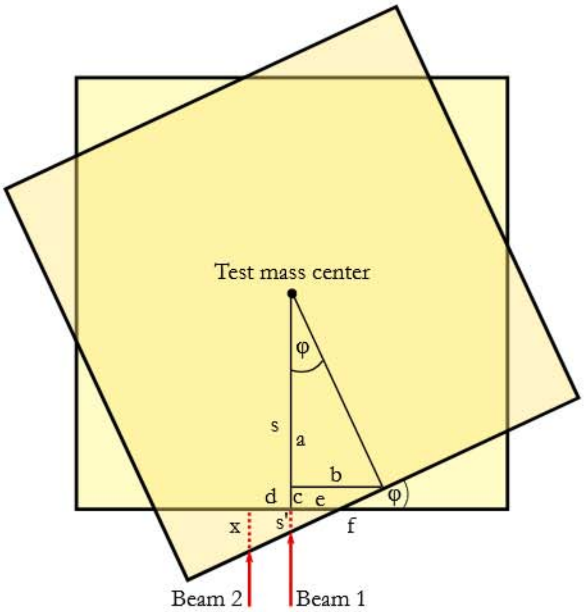

Figure 7.2: The test mass is tilted by ϕ causing a change in the optical path of the beams. Beam 1 is hitting the test mass in the center line and only experiences a second order length change. Beam 2 is additionally misaligned by d and sees therefore an additional linear shift. Both these shifts affect the lever arm by only a small amount (for the requirements here).

Assuming 10 μm misalignment for d it can be estimated that the lever arm is only reduced by ~8 nm for a maximum tilt of 500 μrad and was therefore neglected.

7.1.4 Lever arm effect

For the lever arm effect it was assumed that the pivot point of the test mass was always at the point of incidence. It has had to be taken into account that the reflected beam changes by twice the angle of the test mass tilt (also known as beam angle doubling).

Note that the second lever arm (from test mass two to the photodiode) could be defined as

$$s_2 = \begin{cases} \frac{s_2^A + s_2^B}{2}, & \text{Balanced detection active,} \\ s_2^A, & \text{Balanced detection inactive, only DMU side A active,} \\ s_2^B, & \text{Balanced detection inactive, only DMU side B active,} \end{cases} \tag{7.2}$$

due to the different distances, where the superscripts A and B denote the DMU side which was not masked. However, throughout the actuation scheme only the average was used, and the missing ≈11 mm were neglected.

When both test masses were tilted, a small angle approximation gives

$$\text{Beamwalk on PD12} \approx \underbrace{2\phi_1 s_1}_{\text{Beamwalk on TM2}} + \underbrace{(2\phi_1 - 2\phi_2) s_2}_{\text{Beamwalk after reflection from TM2}} . \tag{7.3}$$

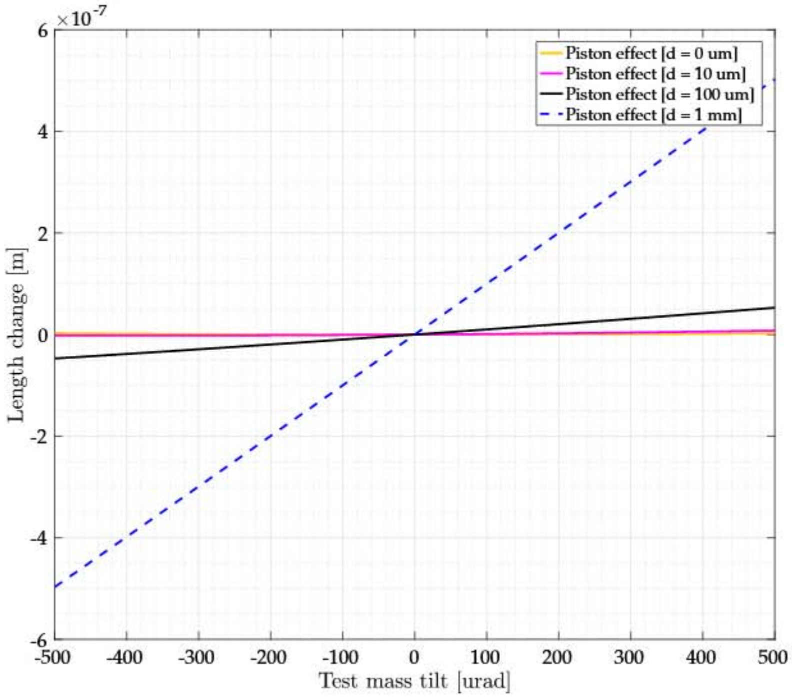

Figure 7.3: Shown is the path length change due to the piston effect for various beam alignments. The magnitude of this effect is well below the lever arm difference in the balanced detection scheme of ∼11 mm.

To minimize the beam walk we found

$$\text{beamwalk on PD12} \overset{!}{=} 0 \quad \Rightarrow \quad 2\phi_1(s_1+s_2) = 2\phi_2 s_2 \tag{7.4}$$

$$\Rightarrow \phi_1 = \frac{s_2}{s_1+s_2}\phi_2 \approx 0.270366\ \phi_2. \tag{7.5}$$

This means the test masses were to be tilted in the same direction if beam offsets were supposed to cancel out and that the first test mass needed to be tilted by a fraction of the tilts of test mass two. For the given setup the factor was $s_2/(s_1+s_2) \approx 0.27$.

7.1.5 Simulation

For the investigation the parameter space was sampled by a spiral with the boundary conditions given above.

Figure 7.4 shows the simulated steps in the parameter space in terms of electrical phases as the photodiodes would measure them.

7.1.6 Schedule

Every measurement point required separate test mass one (η_1, ϕ_1) and test mass two (η_2, ϕ_2) actuation. While measuring, there was a certain time when the B side diodes were masked, so that only the A side diodes were active. This was required for every measurement point.

The schedule was as follows. Start at 8.00 h and do for all set-points:

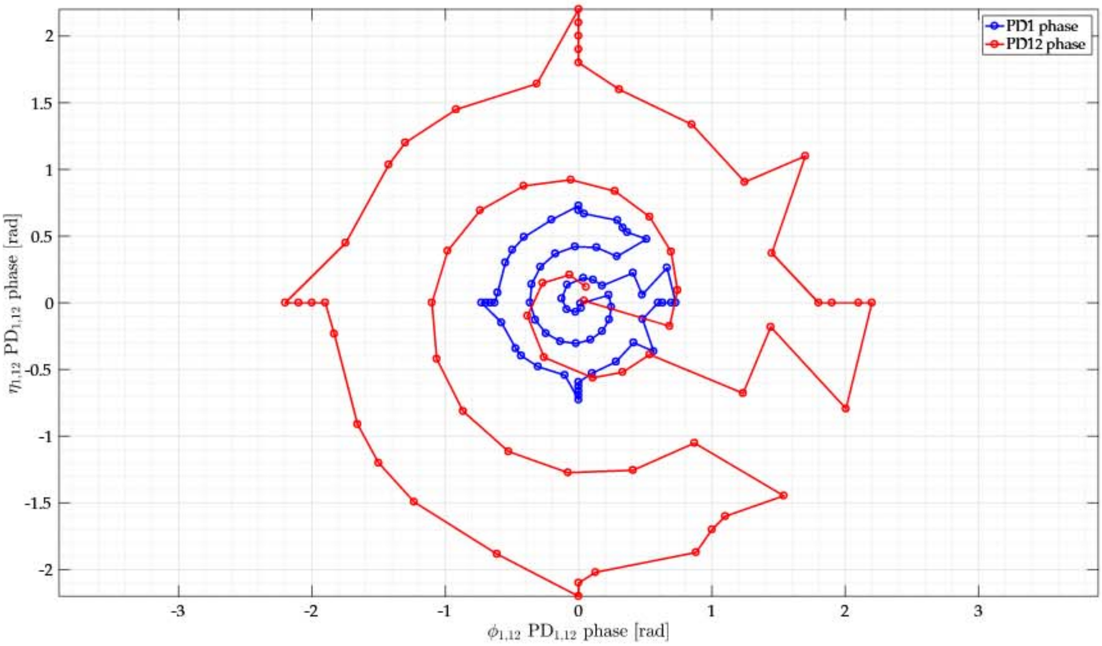

Figure 7.4: Shown is the phase spiral commanded in the second DWS step experiment. The commanded set points are shown as circles and the connecting lines were expected to be extended by the actual test mass trajectories leading to overshoots. These had to be taken into account to avoid too large offsets through careful design.

- Actuation command from current set-point to next set-point
- Wait for 30 min for TMs to stabilise
- Wait another 7 min for taking data
- If measurement point marked as B-IDL record all four DWS channels as IDL packages for 120 s.
- If measurement point marked as B-IDL stop recording IDL and transfer the IDL data.
- Mask B diodes.
- Wait 1 min
- If measurement point marked as U-IDL record all four DWS channels as IDL packages for 120 s.
- If measurement point marked as U-IDL stop recording IDL and transfer the IDL data.
- Wait for another 7 min for taking data
- Unmask B diodes (balanced detection enabled)

The IDL packages contained data with a sampling frequency of 100 Hz and can be used to analyse aliasing effects.

The DFACS DWS PREPROC offsets were set to

$$\phi_{1,\text{offset}}^{\text{PREPROC}} = -61.2\,\mu\text{rad} \tag{7.6}$$
$$\eta_{1,\text{offset}}^{\text{PREPROC}} = -4.9\,\mu\text{rad} \tag{7.7}$$
$$\phi_{2,\text{offset}}^{\text{PREPROC}} = -9.7\,\mu\text{rad} \tag{7.8}$$
$$\eta_{2,\text{offset}}^{\text{PREPROC}} = -3.3\,\mu\text{rad} \tag{7.9}$$

during the experiment and have been confirmend by measurements. They were used to update the slew table:

$$\phi_1^{\text{PREPROC}} = \phi_1^{\text{DWS}} - \phi_{1,\text{offset}}^{\text{PREPROC}} \tag{7.10}$$
$$\eta_1^{\text{PREPROC}} = \eta_1^{\text{DWS}} - \eta_{1,\text{offset}}^{\text{PREPROC}} \tag{7.11}$$
$$\phi_2^{\text{PREPROC}} = \phi_2^{\text{DWS}} - \phi_{2,\text{offset}}^{\text{PREPROC}} \tag{7.12}$$
$$\eta_2^{\text{PREPROC}} = \eta_2^{\text{DWS}} - \eta_{2,\text{offset}}^{\text{PREPROC}} \tag{7.13}$$

With these updates the new investigation design was directly discussed and implemented in agreement with the STOC team at ESOC, Darmstadt.

7.1.7 LTP parameters

The main LTPDA parameters were the following

`LTPDATelemetry.DMU_OMS_DWS_eta1`, `LTPDATelemetry.DMU_OMS_DWS_phi1`, `LTPDATelemetry.DMU_OMS_DWS_eta2`, `LTPDATelemetry.DMU_OMS_DWS_phi2`, `LTPDATelemetry.DMU_OMS_CONTRAST_1`, `LTPDATelemetry.DMU_OMS_CONTRAST_12`.

In nominal DFACS science mode SCI1.2 and activated SDM19 the data was available with sampling frequencies of 1 Hz and 10 Hz. It was preprocessed with the usual procedures and split according to the investigation timeline.

In general the noise behaviour of both angular alignments was analysed and compared with the model expectations and the previous experimental results. It is important to find and define stable segments especially in the presence of possible transients originating from the masking procedures. This data is still under review for future publications.

7.1.8 Results

The experiment was run on 02.06.2017 starting at 23.00h. However, due to a failure in a preceding experiment test mass 2 was not at its zero position, but remained rather at an offset of 275 nm. This may have had an influence of the evaluation of RIN coupling. Additionally, it is unclear at the time of writing how the performance of the DFACS controller is changing due to the shifted position and its impact on the experiment.

Figure 7.5 presents the measured time series of all DWS channels. It can be seen that the slews were much larger than in the previous experiment and that both test masses were actuated in parallel. The times at which IDL data was taken have been masked out, because the procedure creates transients in some channels. Apart form the aforementioned configuration, the experiment was run as planned.

Figure 7.6 shows the impact of the experiment in the longitudinal channels. The small slews on test mass 1 have basically no visible impact. The more precise measurement of the differential displacement shows a varying o_{12} signal. It can be used to characterise the o_{12} noise and its dependence on the contrast. The source of the larger transients in o_{12} is still under investigation.

The contrast itself in X1 and X12 is shown in Figure 7.7 and in combination over the parameter space in Figure 7.8. We can see that the contrast never dropped below 25 %. It stayed in the range 80.9 % to 96.8 % in X1 and between 25.2 % to 98.7 % in X12. This can be attributed to the actuation scheme designed specifically for this experiment. The test mass 1 slews compensated the effect of the larger test mass 2 tilts which led to an overall reduced angular phase measurement on the PD12 diodes.

Looking closely at the segments, as given in Figure 7.9, one finds that the test mass 2 did not completely stabilise before the B side was masked. The reason for this behaviour is still under investigation. The masked period is highlighted in black and shows a jump or drop in the angular and longitudinal measurements. It is in the order of 5 % for the contrast. The reason for this is still under investigation.

The noise over phase dependency in DWS is confirmed over a wider range as before, and it supports the theory of a sinusoidal systematic in the coupling. The measurement time was relatively short to measure as many points as possible along this slope. It is currently unknown why the high frequency noise was not as white as expected, which is subject to ongoing investigations.

7.1.9 Summary

The aim of this experiment was to measure the noise floor within the DWS signals for a range of test mass alignments to improve our understanding on the requirements of the LISA point ahead configuration noise budget. Compared to the previous experiment this investigation targets a verification of the RIN contribution at large test mass tilts.

To come close to the LISA configuration both test masses were tilted in the same direction to avoid beam walk effects on the quadrant photodiodes. For this, test mass 1 needed to be tilted by about a factor of 0.27 of the test mass 2 tilt due to the longer lever arm. At the same time phase wraps are avoided to occur at $\pm\pi$ in the raw DWS signal due to non-existing phase tracking.

During the measurement phase of the set-points DMU B side diodes were masked for a certain amount of time so that only A side diodes were active and measuring (this causes balanced detection to fail). It was switched back for the next set-point, and repeated.

The measurement timespans themselves were in the order of minutes, for the interest lays in the high frequency data (1 Hz to 4 Hz). A big drop in contrast was expected in the worst case (eventually down to 10%), but the OMS sensing remained functional in this case, and the contrast stayed above any critical value for the whole experiment.

The investigation lasted for roughly ~48 h. The experimental analysis is still on-going, and is expected to give insights in the RIN behaviour over the whole mission, as found in similar fashion in the longitudinal test mass scans (described in Section 6).

The experiment confirms the so far unmeasured RIN coupling from twice the heterodyne frequency in DWS over a wider range of phase offsets. It also gives reason to continue research in this direction, since the unbalanced coupling was expected to behave in a slightly different

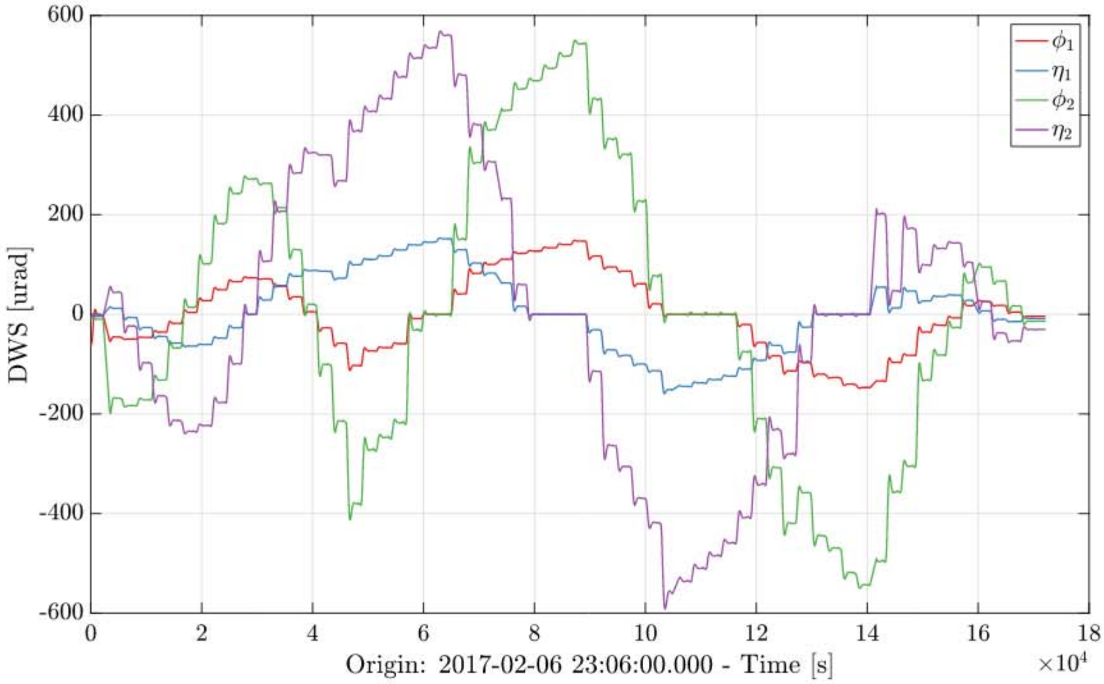

Figure 7.5: Timeseries of the second DWS experiment. Shown are the four test mass angles as measured by DWS through the OMS. The different set points of the test mass angles can be observed. There is always a small overshoot until the test mass settles on the new set point.

manner and the test masses stabilised slower than during the first experiment. The overall noise level appears to be slightly higher, with more high frequency noise components being present. The analysis of this data and noise modelling is ongoing in the AEI.

7.2 DWS de-risk slews in-orbit

7.2.1 Investigations

On DOY17 in 2017 specific de-risk investigations were run to ensure the spacecraft behaves in a controllable way for large test mass slews.[2]

It was important to avoid raising safety flags on the satellite due to low contrast in the OMS or switching to DC control instead of DWS based control. Also, the phase tracking algorithm which is available in the longitudinal interferometers had not been applied for DWS signals. Therefore, possible phase jumps had to be avoided. The new design involved switching between measurement diodes therefore possible transient effects due to sudden losses of signals had to be considered, too.

All of this was addressed with a specific investigation that is described in the following. The design of the second DWS step experiment was adjusted accordingly.

In the de-risk procedures the test masses were misaligned up to 1000 μrad which had to

---

[2] These information can also be found in the appendix of [19].

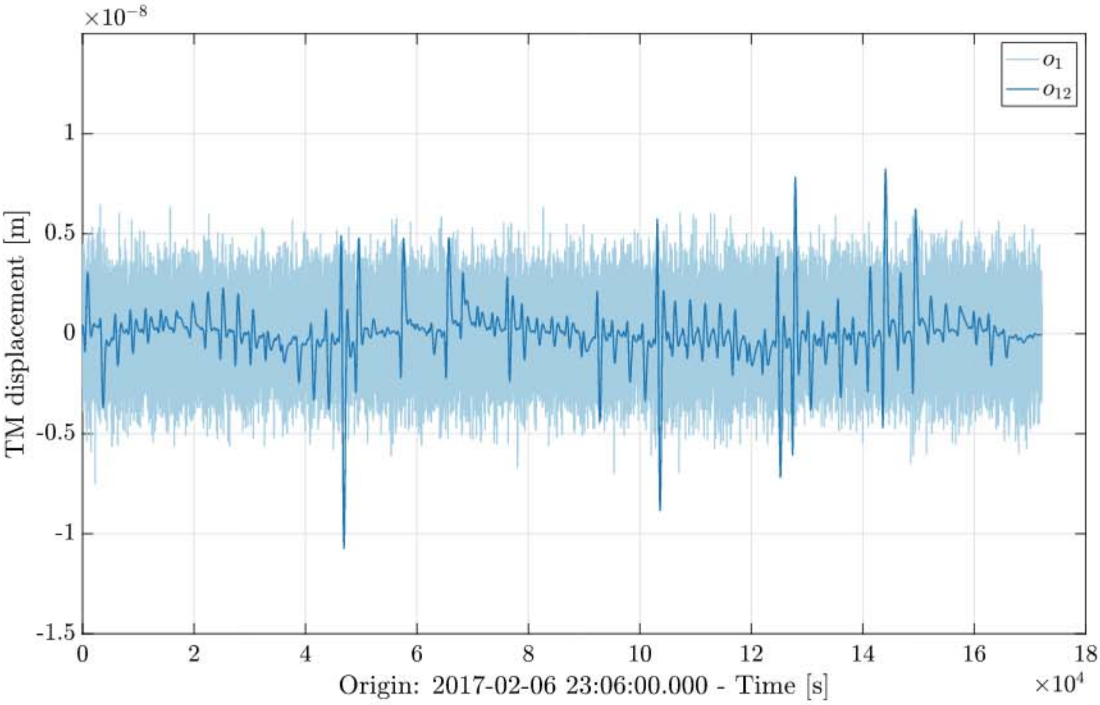

Figure 7.6: Timeseries of o_1 and o_{12}. The first measurement is dominated by noise, while the more precise data of o_{12} shows an effect of the test mass slews. The mean values have been subtracted. Test mass 2 was offset at 275 nm due to a failure in a preceding experiment. The large transients in o_{12} are still under investigation.

be done in DFACS mode ACC3, using GRS for suspension control. The exact commanding was, starting at 2017-01-17 08:30:00 UTC:

(1) η_1 sine wave, 1 period, amplitude 1 mrad.

(2) ϕ_1 sine wave, 1 period, amplitude 1 mrad.

(3) η_2 sine wave, 1 period, amplitude 1 mrad.

(4) ϕ_2 sine wave, 1 period, amplitude 1 mrad.

(5) Slew η_2 to 600 μurad, ϕ_2 to 600 μrad.

(6) Slew η_1 to 162 μrad, ϕ_1 to 162 μrad.

(7) Slew η_1 to 600 μrad, ϕ_1 to 600 μrad.

(8) Slew η_2 to -600 μrad, ϕ_2 to -600 μrad.

(9) Slew η_1 to -162 μrad, ϕ_1 to -162 μrad.

(10) Slew η_1 to -600 μrad, ϕ_1 to -600 μrad.

(11) Slew η_1 to 0 μrad, ϕ_1 to 0 μrad, η_2 to 0 μrad, ϕ_2 to 0 μrad.

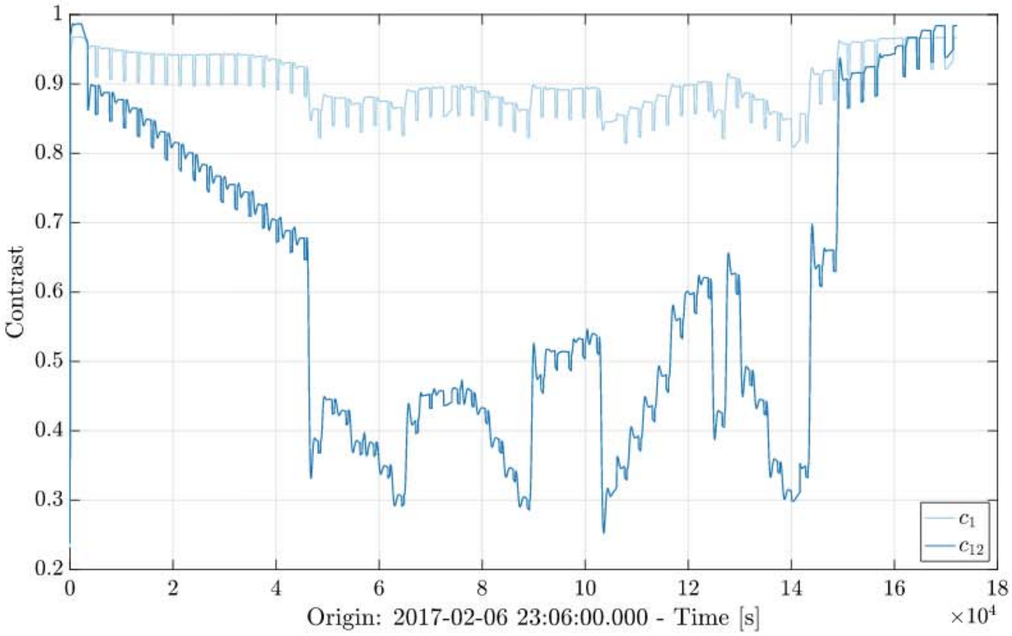

Figure 7.7: Timeseries of the contrast in both test mass interferometers. Transients due to IDL switching have been removed. The visible small drops coincide with the masking of the B side photodiodes.

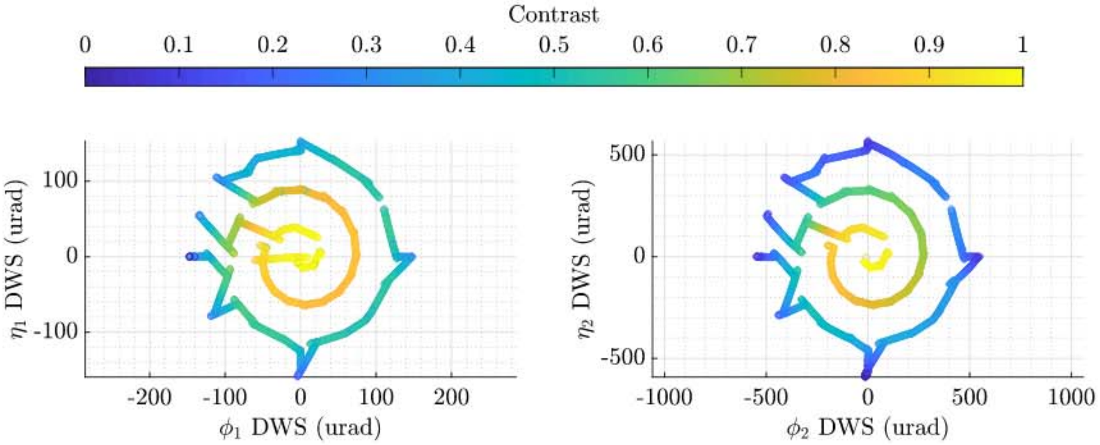

Figure 7.8: The parameter space in DWS as measured by the OMS. Segments containing transients due to IDL switching have been masked out. The resulting contrast stays above 25 % for the contrast in X12, and above 80 % for the X1 interferometer for the whole experiment.

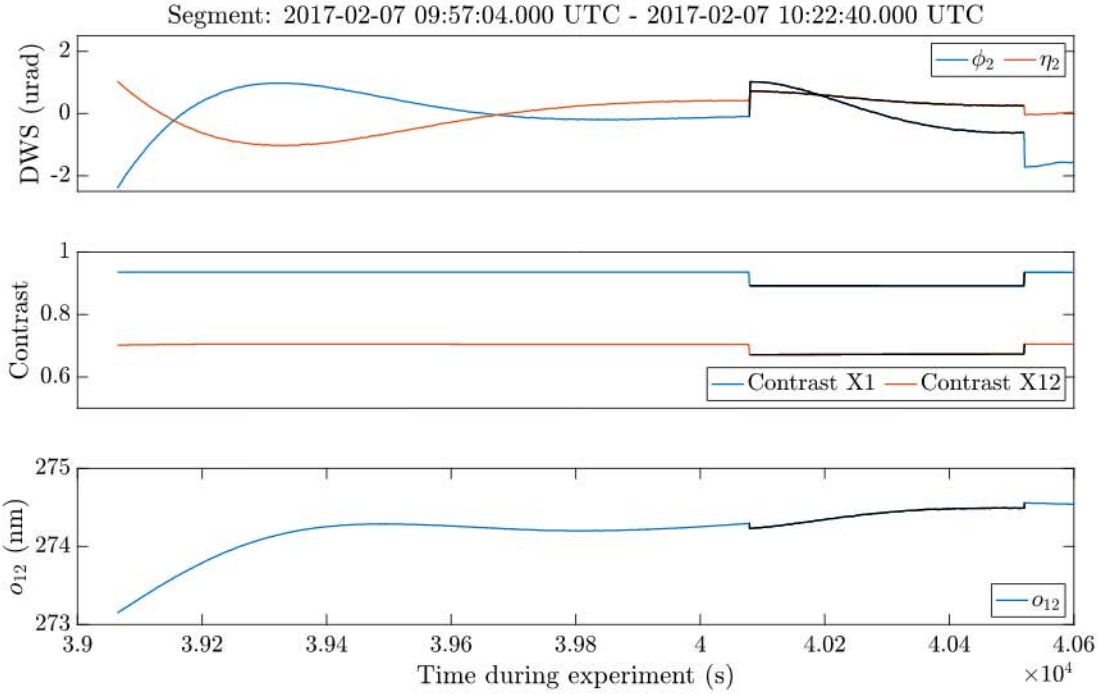

Figure 7.9: A zoomed view of one of the set points. It can be seen that the test mass did not fully stabilize before the B side diodes were masked (masked time is marked in black). The top plot has the segment means subtracted.

Each of the sine wave injection lasted for 1 h. The slew commands were separated by 30 min and started two minutes after the last sine wave was finished. Figure 7.10 shows all four channels of GRS and DWS readout. The contrast is shown in Figure 7.11.

Crosstalk from test mass one into test mass two DWS readout: Cross talk from phase jumps were only happening when the PD1 or PD12 phase was close to π rad. In the DWS experiment, PD1 did not reach these values. The following extremal values were set, resulting in crosstalk:

- `DMU_DWS_phi2`: Maximal slew of 543.57 μrad – at 540 μrad (phase jump while $\phi_1 = -62\,\mu$rad) with a large crosstalk into η_2 of 155 μrad.
- `DMU_DWS_phi2`: Minimal slew of $-543.57\,\mu$rad with a maximal crosstalk into $\eta_2 = -3.75\,\mu$rad.
- `DMU_DWS_eta2`: Maximal slew of 560.87 μrad with a maximal crosstalk into $\phi_2 = -20\,\mu$rad.
- `DMU_DWS_eta2`: Minimal slew of $-560.87\,\mu$rad with a maximal crosstalk into $\phi_2 = -37\,\mu$rad.

These crosstalk effects can be used to characterize GRS and DWS readout at larger misalignments, which is planned as future work.

While transitioning back to SCI1.2 (during which SCI1.1 was active) a photodiode masking test procedure was performed. It is shown in Figure 7.12 how the contrast shows a step

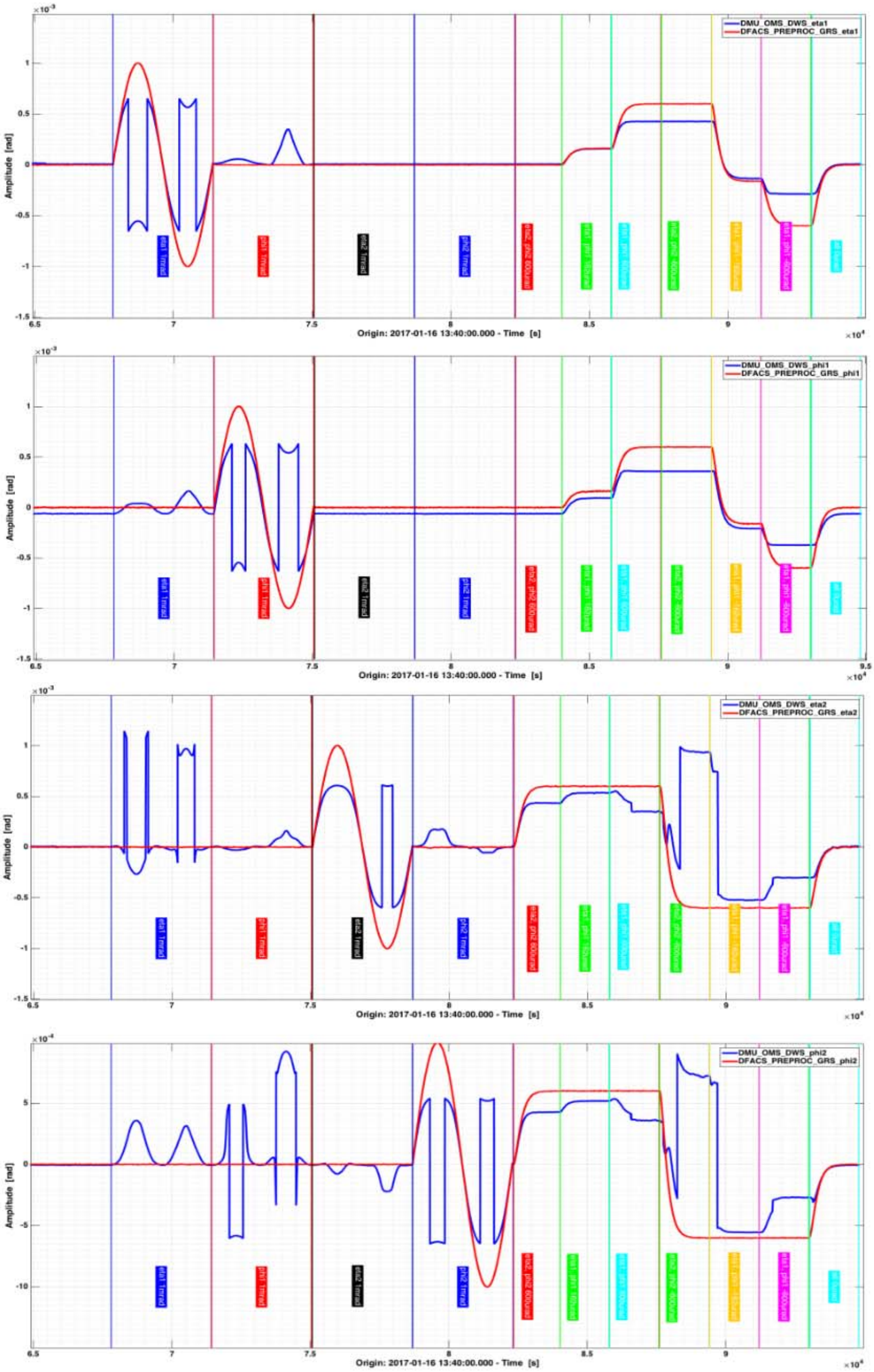

Figure 7.10: The de-risk investigation slews are shown over time. It was important to avoid the phase jumps visible here.

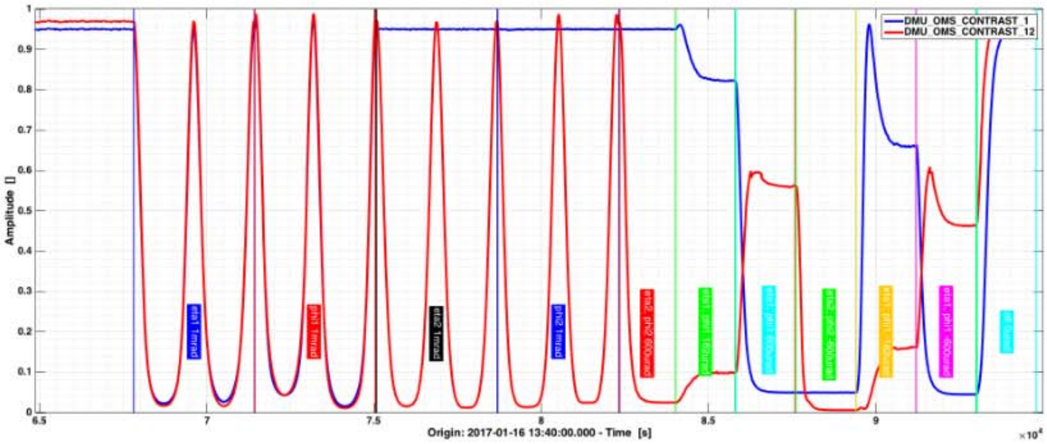

Figure 7.11: The de-risk investigation slews are heavily influencing the contrast. At 5 % level a DWS unavailability flag is raised, which needed to be avoided.

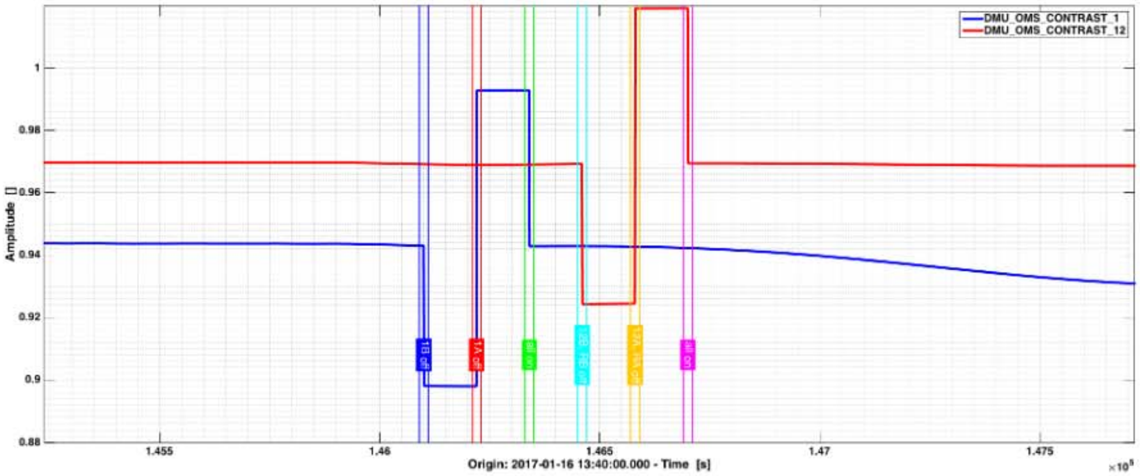

Figure 7.12: The contrast shows a large step response after masking different photodiodes.

response due to its DC dependence. The DWS response is shown in Figure 7.13. It is generally very small in the order of 1 μrad such that the slow controller response won't cause fast or large drifts.

7.2.2 Wide-range mode analysis

The main results can be summarized as follows:

- The beamwalk compensation scheme worked and improved the contrast.
- Another benefit of this scheme was that it avoided phase jumps that would have happened if test mass one was not actuated simultaneously.

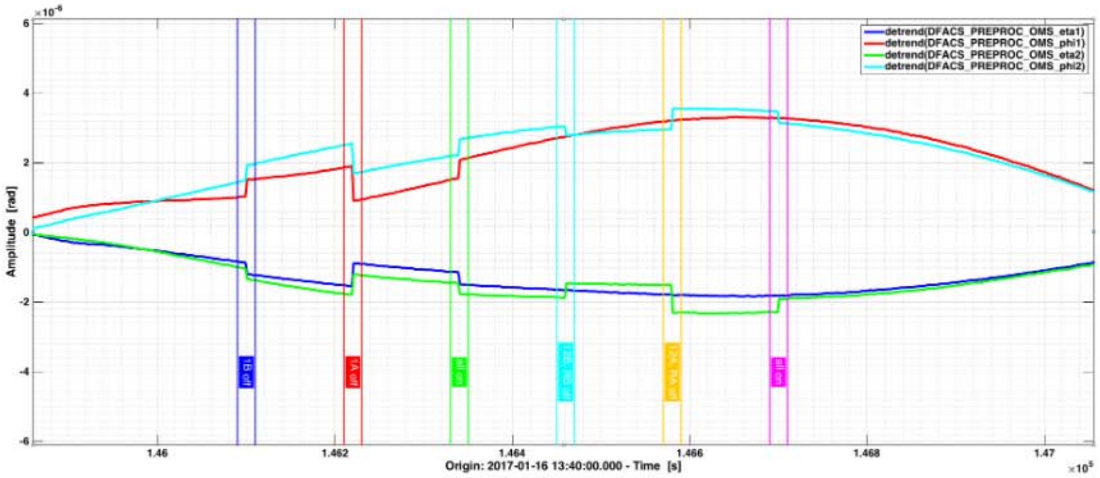

Figure 7.13: The response of the DWS readout is generally very small and will not interfere with the measurement. The long transient is induced by DFACS mode transitions.

- Crosstalk was measured between test mass one to test mass two angles, also between test mass two angles themselves (up to 150 μrad).
- The flags switching from DWS to DC control were advised to be re-set to 3 % to avoid jumps in control.
- Masking B-side photodiodes was rather unproblematic and the largest jumps are in sub-micro-radian level in all four channels. Any slow controller response to these was expected to be below the drift rate in the first step experiment.
- It was important to update the slew table with the correct DWS PREPROC values, which represented any offsets the DFACS controller was using. This avoided potential phase jumps around larger slews.

8 Reference Beam Modulation Experiment

8.1 Scope

The aim of this experiment was to measure the contrast depending on the beam powers and use it to validate our noise model of the OMS.

The investigation reduced the power of the reference beam in a number of set points and reversed the process afterwards.

The investigation was run in two configurations, first (decreasing the beam power) for nominal test mass positions around nominal zero offset, and then (increasing the beam power again) for test mass two at an offset of 133 nm in x direction. The latter should lead to a maximal RIN coupling according to the previous longitudinal test mass shift experiment.

The investigation lasted for roughly 6 hours and for every set-point 100 Hz IDL data was additionally recorded for $\Psi_F, \Psi_R, \Sigma_{12}$ and o_{12}.

8.2 Experimental design

In detail, the procedure was as follows. The spacecraft was operating in DFACS mode Sci 1.2. and the test masses were in their zero position. P_r refers to the reference beam power.

1. P_r set to 100%, record 1000 s and IDL 80 s (at the beginning)
2. P_r set to 90%, record 1000 s and IDL 80 s (at the beginning)
3. P_r set to 85%, record 1000 s and IDL 80 s (at the beginning)
4. P_r set to 80%, record 1000 s and IDL 80 s (at the beginning)
5. P_r set to 70%, record 1000 s and IDL 80 s (at the beginning)
6. P_r set to 60%, record 1000 s and IDL 80 s (at the beginning)
7. P_r set to 55%, record 1000 s and IDL 80 s (at the beginning)
8. P_r set to 50%, record 1000 s and IDL 80 s (at the beginning)
9. P_r set to 40%, record 1000 s and IDL 80 s (at the beginning)
10. P_r set to 30%, record 1000 s and IDL 80 s (at the beginning)

Then, test mass 1 was kept at zero position, but test mass 2 was set to $x = 133\,\text{nm}$, followed by a 30 min wait for test mass 2 to reach the new position and stabilise. Afterwards, the previous steps were run in reverse:

1. P_r set to 30%, record 1000 s and IDL 80 s (at the beginning)

2. P_r set to 40%, record 1000 s and IDL 80 s (at the beginning)
3. P_r set to 50%, record 1000 s and IDL 80 s (at the beginning)
4. P_r set to 55%, record 1000 s and IDL 80 s (at the beginning)
5. P_r set to 60%, record 1000 s and IDL 80 s (at the beginning)
6. P_r set to 70%, record 1000 s and IDL 80 s (at the beginning)
7. P_r set to 80%, record 1000 s and IDL 80 s (at the beginning)
8. P_r set to 85%, record 1000 s and IDL 80 s (at the beginning)
9. P_r set to 90%, record 1000 s and IDL 80 s (at the beginning)
10. P_r set to 100%, record 1000 s and IDL 80 s (at the beginning)

Afterwards, test mass two was set back to its nominal position.

8.3 Contrast

With a simple model, the contrast change was expected to behave roughly according to $2\sqrt{(P_m * P_r)/(P_m + P_r)}$, where P_m is the power of the measurement beam and P_r the power of reference beam [22]. When keeping P_m constant, P_r can be reduced by steps down to approximately 30 % of its original power as it was estimated from another experiment during the main mission. Figure 8.1 shows the prediction for the contrast during this experiment.

8.4 Analysis

The data of the experiment is shown in Figure 8.2. It can be seen that only the reference beam power was modulated. In Figure 8.3 the measurement of the second power monitor diode is showing an approximately linear behaviour that is offset to a previous investigation.

The effect of moving the test mass 2 to a new operating point halfway through the experiment can be seen in Figure 8.4. It is clearly visible that the position at 132 nm increases the noise level which was expected.

Using each of the set points to measure this noise level we find the results as given in Figure 8.5. The investigation of these results is still ongoing and planned to be published in a future paper.

Similarly, the experiment can be used to analyse the behaviour of the contrast. A preliminary, simple model that neglects actual beam parameters is already showing a qualitative agreement with the observed behaviour. This can be seen in Figure 8.6.

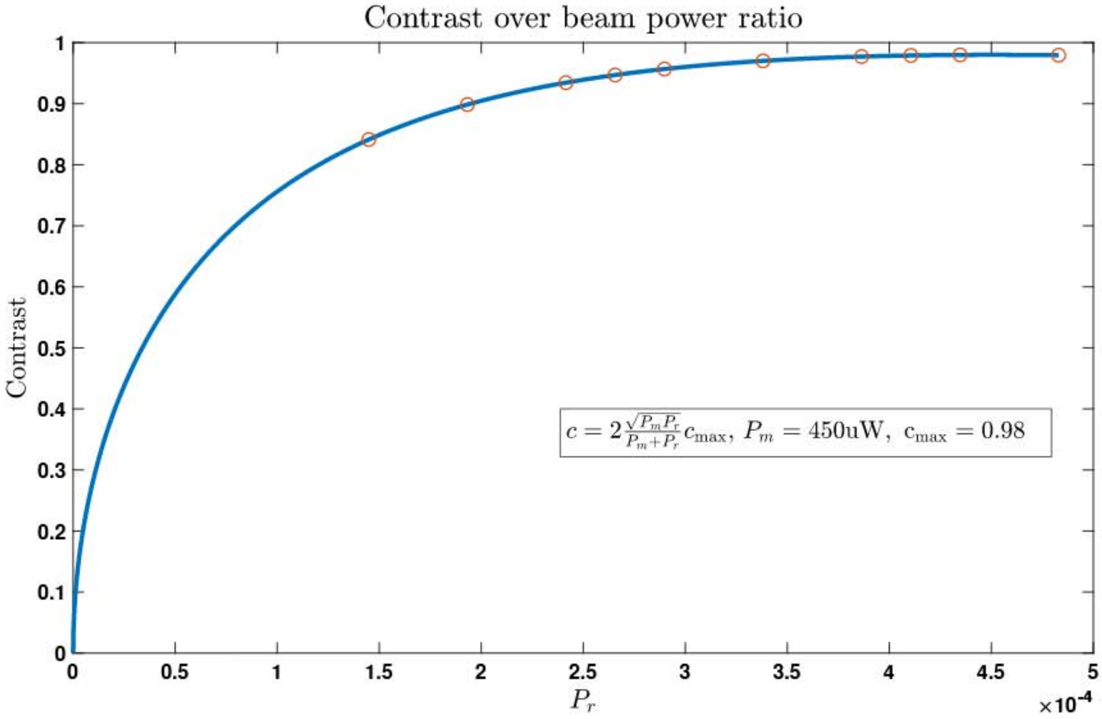

Figure 8.1: Expectation of the contrast behaviour during the experiment. The red circles indicate the set points where the measurement was performed.

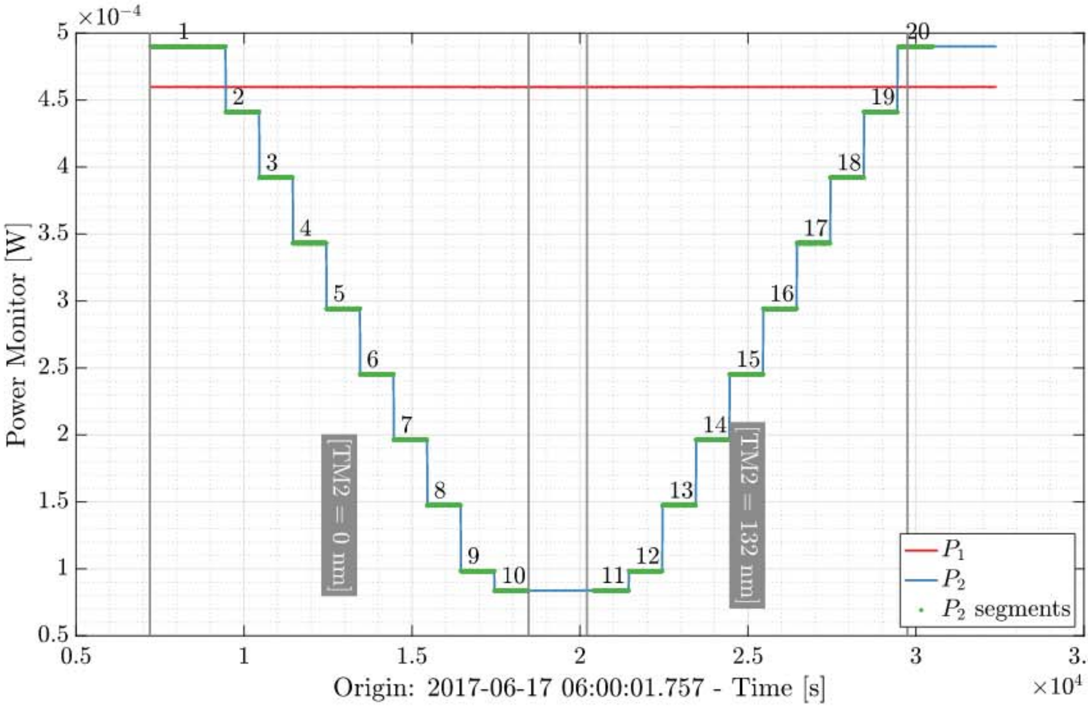

Figure 8.2: Timeseries of the power monitor diodes. It shows that the measurement beam was not modulated. The reference beam diode shows the set points as planned. The segments used for further analysis are marked.

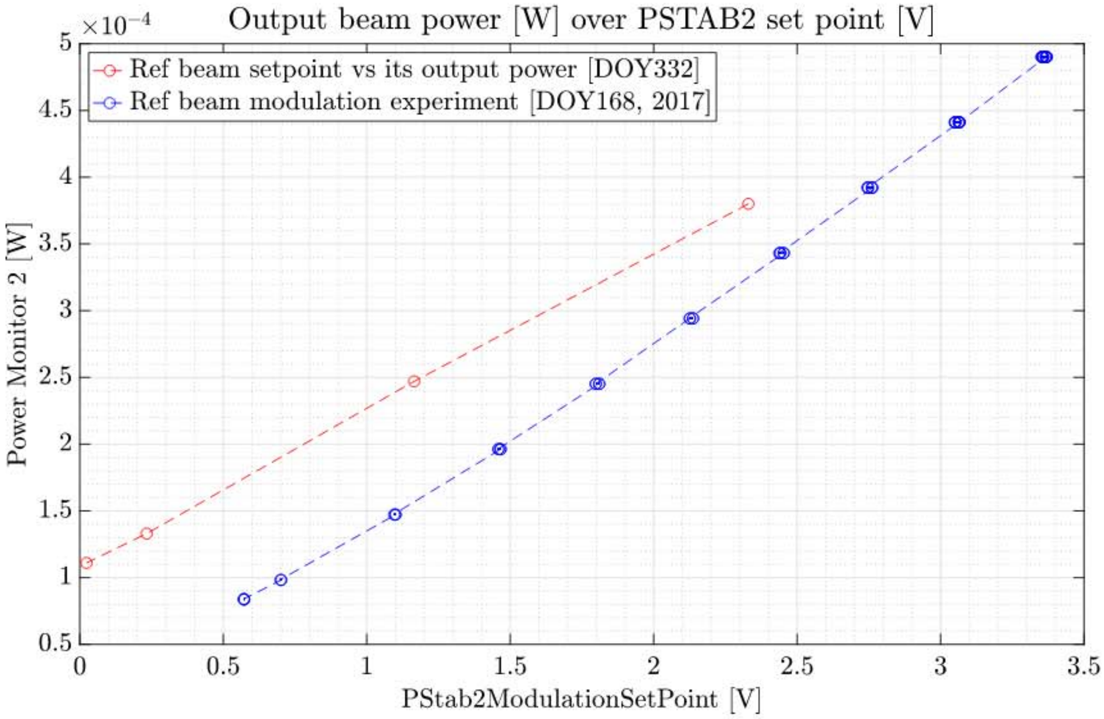

Figure 8.3: A comparison of the controller behaviour to a previous experiment that was run on DOY 332. The measured output power appears to follow a linear slope, while being offset to the compared data.

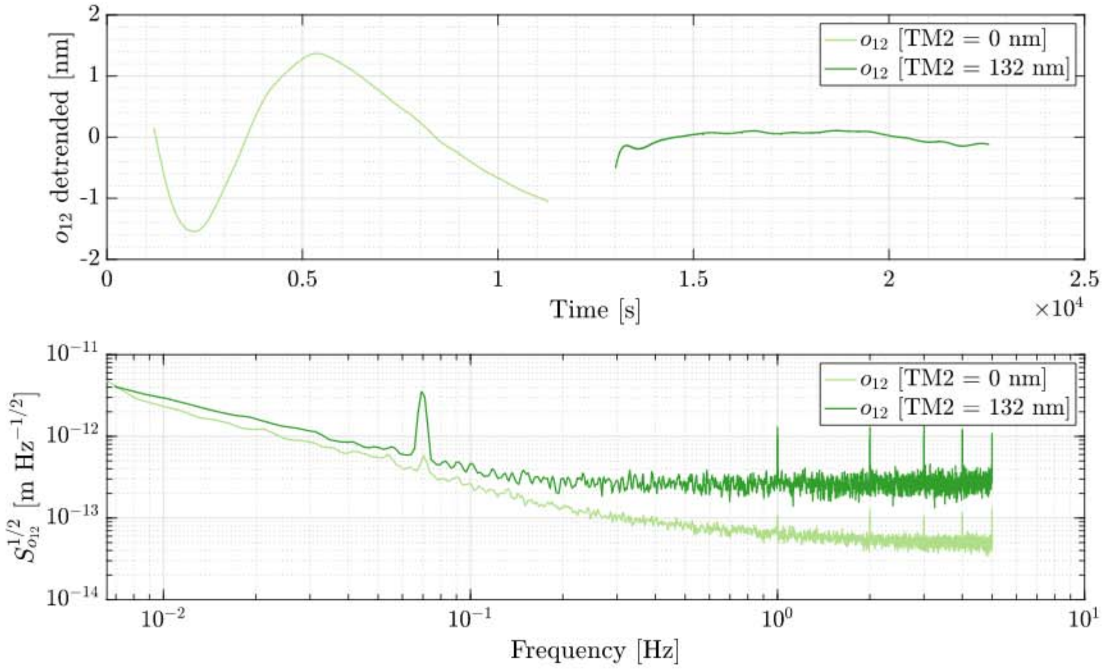

Figure 8.4: The top plot shows the detrended o12 variation during the experiment. The bottom panel shows the resulting spectra for each of the two time segments.

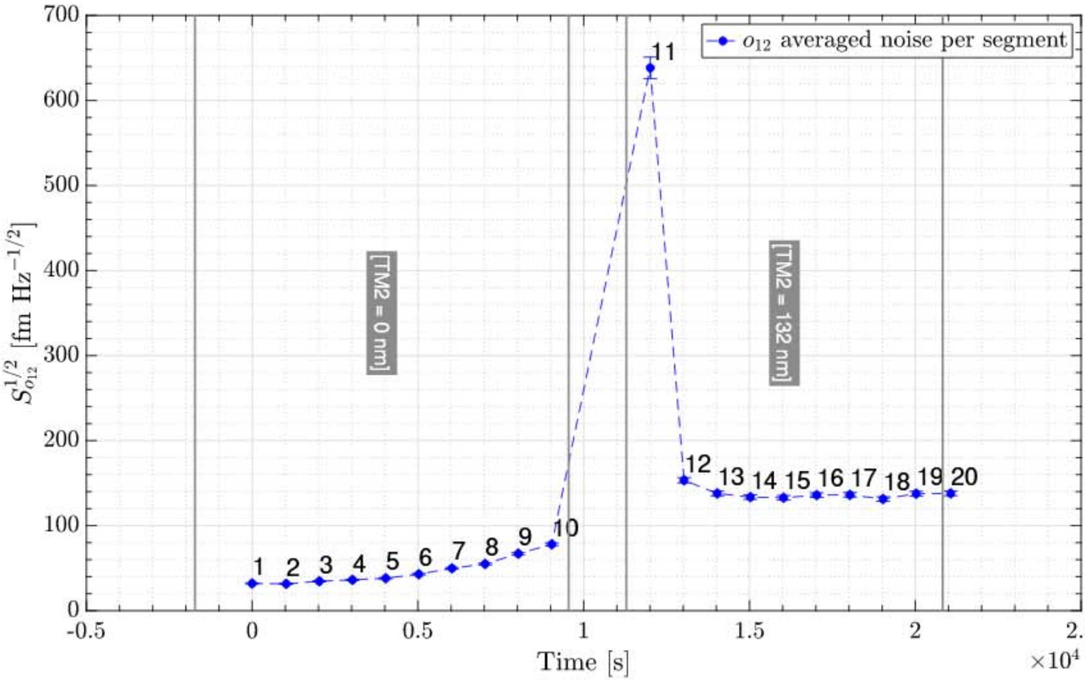

Figure 8.5: Shown is the measured noise over the time of the experiment. The points correspond to a measurement in one of the marked segments as shown in Figure 8.2. It can be seen that the measured noise level changes for each set point. The large outlier, labelled as segment number 11, is still under investigation.

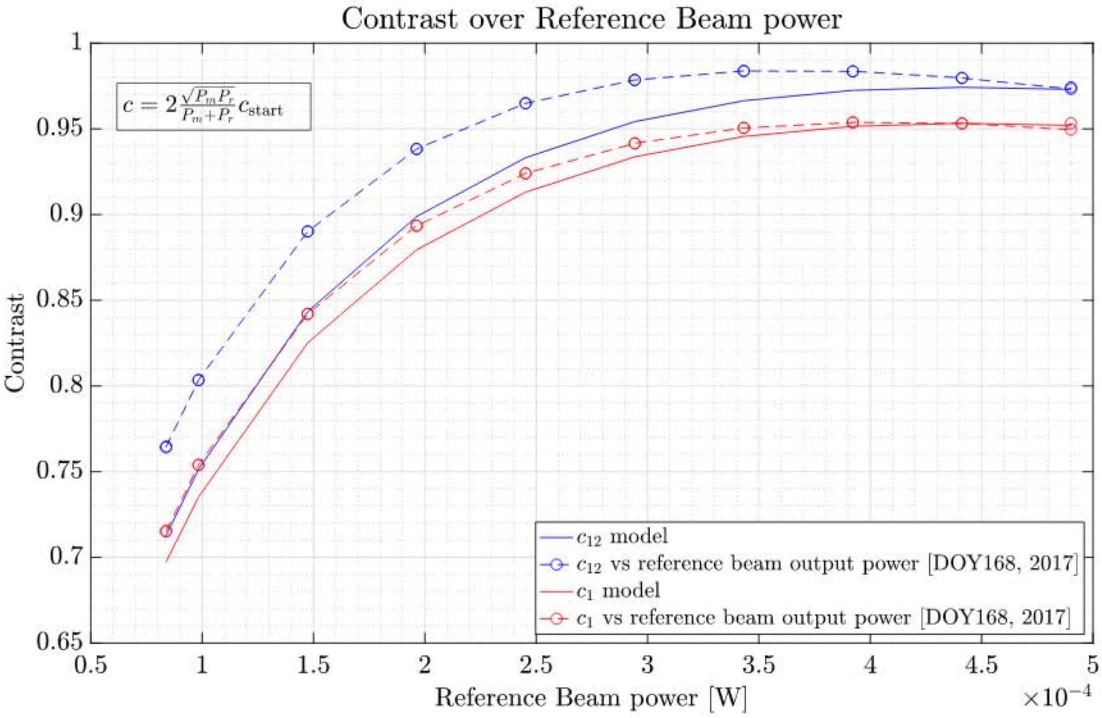

Figure 8.6: The measured maximal contrast per segment (transients due to IDL switching have been ignored) and a simple model based on the contrast have been applied. The discrepancy is likely due to actual beam alignment and orientation between the incoming wavefronts. A more detailed analysis including a more sophisticated model is in preparation.

9 OPD investigations

As described in the OMS introduction of [1] the output of the reference interferometer Ψ_{R} is used for two purposes.

Because it describes the Optical Pathlength Difference (OPD) between the reference and the measurement beam it is used as the error point for the OPD control loop which keeps this difference close to zero. Furthermore, the remaining pathlength difference is common to all interferometers and therefore is subtracted from their Ψ_{F}, Ψ_1 and Ψ_{12} outputs.

During the mission characterisation experiments of the OPD loop were performed regularly as part of the monitoring of the OMS. For these experiments guidance signals at different frequencies were injected. The time series of such experiment performed on DOY027 can be seen in Figure 9.1. By recording the response signals to these injections the transfer function of the control loop was estimated. The included gain factor of the piezo pathlength actuators could be verified to not degrade over the extended mission.

Further investigations, of which the analyses have not been finished and published yet, include the pathlength noise over the mission time and the OPD noise coupling into the other interferometers.

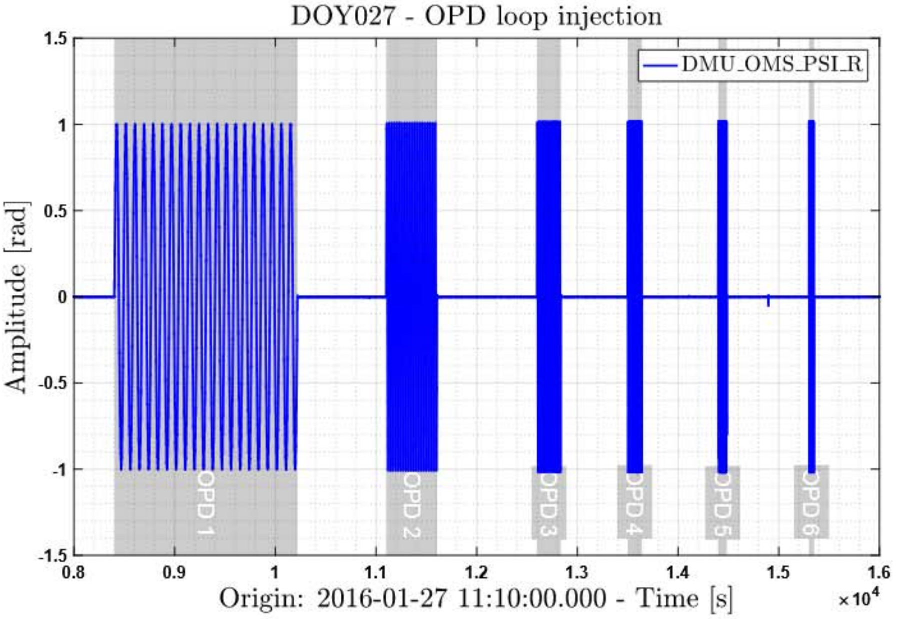

Figure 9.1: Time series of the OPD guidance injections, sine wave at 6 frequencies were injected to characterise the OPD loop.

Acknowledgements

This work has been made possible by the LISA Pathfinder mission, which is part of the space-science program of the European Space Agency. We acknowledge the support of the German Space Agency, DLR. The work is supported by the Federal Ministry for Economic Affairs and Energy based on a resolution of the German Bundestag (FKZ 50OQ0501 and FKZ 50OQ1601). The following industries have supplied an excellent hardware under this grant: Airbus DS GmbH in Friedrichshafen, OHB-System AG in Munich (previously Kayser-Threde GmbH) and TESAT Spacecom Gmbh & Co. KG in Backnang.

The French contribution has been supported by CNES (Accord Specific de projet CNES 1316634/CNRS 103747), the CNRS, the Observatoire de Paris and the University Paris-Diderot. E. Plagnol and H. Inchauspe would also like to acknowledge the financial support of the UnivEarthS Labex program at Sorbonne Paris Cité (ANR-10-LABX-0023 and ANR-11-IDEX-0005-02). The Italian contribution has been supported by Agenzia Spaziale Italiana and Istituto Nazionale di Fisica Nucleare. The Spanish contribution has been supported by Contracts No. AYA2010-15709 (MICINN), No. ESP2013-47637-P, and No. ESP2015-67234-P and No. ESP2017-90084-P (MINECO), and 2017-SGR-1469 (AGAUR). M. Nofrarias acknowledges support from Fundacion General CSIC (Programa ComFuturo). F.Rivas acknowledges support from a Formacion de Personal Investigador (MINECO) contract. The Swiss contribution acknowledges the support of the Swiss Space Office (SSO) via the PRODEX Programme of ESA. L. F. acknowledges the support of the Swiss National Science Foundation Project Number 200021-162449. The UK groups wish to acknowledge support from the United Kingdom Space Agency (UKSA), the University of Glasgow, the University of Birmingham, Imperial College, and the Scottish Universities Physics Alliance (SUPA). J. I. Thorpe and J. Slutsky acknowledge the support of the U.S. National Aeronautics and Space Administration (NASA).

List of Figures

List of Tables

Bibliography

[1] K. Danzmann, G. Heinzel, M. Hewitson, J. Reiche, M. Tröbs, G. Wanner, et al.: "LPF final report for the German contribution to the nominal mission"; 2018.

[2] M. Armano, H. Audley, G. Auger, J. T. Baird, M. Bassan, P. Binetruy, et al.: "Sub-Femto-g Free Fall for Space-Based Gravitational Wave Observatories: LISA Pathfinder Results"; *Physical Review Letters*, 116(23):231101, 2016.

[3] M. Armano, H. Audley, J. Baird, P. Binetruy, M. Born, D. Bortoluzzi, et al.: "Beyond the Required LISA Free-Fall Performance: New LISA Pathfinder Results down to 20 μHz"; *Physical Review Letters*, 120(6), 2018.

[4] P. McNamara, S. Vitale, and K. Danzmann: "LISA Pathfinder"; *Classical and Quantum Gravity*, 25(11):114034, 2008.

[5] P. Amaro-Seoane, H. Audley, S. Babak, J. Baker, E. Barausse, P. Bender, et al.: "Laser Interferometer Space Antenna"; *arXiv preprint arXiv:1702.00786*, 2017.

[6] M. Armano, H. Audley, G. Auger, J. T. Baird, P. Binetruy, M. Born, et al.: "Charge-induced force noise on free-falling test masses: Results from LISA Pathfinder"; *Physical Review Letters*, 118:171101, 2017.

[7] M. Armano, H. Audley, G. Auger, J. Baird, M. Bassan, P. Binetruy, et al.: "Capacitive sensing of test mass motion with nanometer precision over millimeter-wide sensing gaps for space-borne gravitational reference sensors"; *Physical Review D*, 96:062004, 2017.

[8] M. Armano, H. Audley, J. Baird, P. Binetruy, M. Born, D. Bortoluzzi, et al.: "Precision charge control for isolated free-falling test masses: LISA Pathfinder results"; *Physical Review D*, 98:062001, 2018.

[9] J. I. Thorpe, J. Slutsky, J. G. Baker, T. B. Littenberg, S. Hourihane, N. Pagane, et al.: "Micrometeoroid events in LISA Pathfinder"; *The Astrophysical Journal*, 883(1):53, 2019.

[10] M. Armano, H. Audley, J. Baird, M. Bassan, S. Benella, P. Binetruy, et al.: "Characteristics and energy dependence of recurrent galactic cosmic-ray flux depressions and of a forbush decrease with LISA Pathfinder"; *The Astrophysical Journal*, 854(2):113, 2018.

[11] M. Armano, H. Audley, J. Baird, S. Benella, P. Binetruy, M. Born, et al.: "Forbush decreases and <2 day GCR flux non-recurrent variations studied with LISA Pathfinder"; *The Astrophysical Journal*, 874(2):167, 2019.

[12] M. Armano, H. Audley, J. Baird, P. Binetruy, M. Born, D. Bortoluzzi, et al.: "In-flight performance of the LISA pathfinder optical metrology system"; forthcoming.

[13] H. Audley, I. Diepholz, A. García, A. Monsky, M. Nofrarias, and F. Steier: "Report on the OMS FM Phase I test campaign - S2-AEI-TN-3068"; Technical report, Max Planck Institute for Gravitational Physics (Albert Einstein Institute), 2012.

[14] M. Hewitson and P. McNamara: "OSTT data analysis report - S2-EST-TN-3061"; Technical report, European Space Agency, 2013.

[15] S. Paczkowski on behalf of the LPF collaboration: "Laser Frequency Noise Stabilisation and Interferometer Path Length Differences on LISA Pathfinder"; *Journal of Physics: Conference Series*, 840(1):012004, 2017.

[16] M. Armano, H. Audley, J. Baird, P. Binetruy, M. Born, D. Bortoluzzi, et al.: "Calibrating the system dynamics of LISA Pathfinder"; *Physical Review D*, 97:122002, 2018.

[17] M. Armano, H. Audley, J. Baird, P. Binetruy, M. Born, D. Bortoluzzi, et al.: '"LISA Pathfinder Performance Confirmed in an Open-Loop Configuration: Results from the Free-Fall Actuation Mode"; *Physical Review Letters*, 123:111101, 2019.

[18] Gudrun Wanner, Nikolaos Karnesis, and LISA Pathfinder collaboration: "Preliminary results on the suppression of sensing cross-talk in LISA Pathfinder"; *Journal of Physics: Conference Series*, 840(1):012043, 2017.

[19] Lennart Wissel: "In-orbit performance and behaviour of the LISA Pathfinder Optical Metrology System"; Master's thesis, Leibniz Universität Hannover, 2017.

[20] G. Wanner: "Complex optical systems in space: numerical modelling of the heterodyne interferometery of LISA Pathfinder and LISA"; 2010.

[21] http://www.lisa.aei-hannover.de/ifocad/.

[22] G. Wanner and G. Heinzel: "Analytical description of interference between two misaligned and mismatched complete gaussian beams"; *Applied Optics*, 53(14):3043–3048, 2014.